



Algorithm Theoretical Basis Document

Annex D

Infrared Mineral Aerosol Retrieval Scheme (IMARS)

Algorithm version: v7.1

Issued by: DLR / Thomas Offenwanger

Date: 29/02/2024

Ref: C3S2_312a_Lot2_D-WP2-FDDP-

AER_202311_ATBD_Annex_D_IMARS_v3.3_final

Official reference number service contract: 2021/C3S2_312a_Lot2_DLR/SC1



This document has been produced in the context of the Copernicus Climate Change Service (C3S).
The activities leading to these results have been contracted by the European Centre for Medium-Range Weather Forecasts, operator of C3S on behalf on the European Union (Contribution Agreement signed on 22/07/2021). All information in this document is provided “as is” and no guarantee of warranty is given that the information is fit for any particular purpose.
The users thereof use the information at their sole risk and liability. For the avoidance of all doubt, the European Commission and the European Centre for Medium-Range Weather Forecasts have no liability in respect of this document, which is merely representing the author’s view.



Contributors

GERMAN AEROSPACE CENTER (DLR)

1. Thomas Offenwanger
2. Stefanos Samaras
3. Lars Klüser

History of modifications

Version	Date	Description of modification	Chapters / Sections
C3S_312a_Lot5			
2.5	08.10.2018	<ul style="list-style-type: none"> • Adaptation to the new template • Revision of the entire processing chain (debugging) • Refinement of the determining conditions for dust and clouds (IMARS v6.0) 	3, 4
C3S_312b_Lot2			
2.5	25.02.2019	No change This version is up to date	
2.5a	30.04.2019	Small corrections based on review by ASSIMILA (cross-referencing)	
3.0	01.10.2020	<ul style="list-style-type: none"> • Adaptation of the entire processing chain in python programming language, including preprocessing which used to run with reading routines (IDL) of EUMETSAT. • Revision of the entire processing chain 	



		<p>(debugging) in terms of algorithmic/mathematical consistency.</p> <ul style="list-style-type: none"> • Uncertainty revised and refined to cover each optical-depth product and an early stage retrieval uncertainty (discriminant) • Enriched quality flagging with entropy discriminants. • Refinement of the determining conditions for dust and clouds (IMARS v7.0) with probability scaling 	
3.1	31.05.2023	<ul style="list-style-type: none"> • Update to C3S2 template • Summarize ongoing optimization of the post-processing 	Title page, 2 nd page, last page, header, footer New section 4.8
3.2	08.09.2023	<ul style="list-style-type: none"> • Review and update of document to C3S2 guidelines • Improvement of several graphics • Restructuring of sections • Change of numbering styles, citation style, section numbering • Change of reference style, footnotes • Bibliography ordered alphabetically • Added general definitions of aerosol variables • Clarified some paragraphs 	Whole document
3.3	26.01.2024	<ul style="list-style-type: none"> • Removed section 3.3.1 • Updated section 3.2.5 with new v7.1 postprocessing scaling 	List of datasets covered by this document, List of variables used in equations, section



		<ul style="list-style-type: none"> • Added “List of variables used in equations” • Updated IMARS version number 	3.2.5, former section 3.3.1
--	--	---	-----------------------------

List of datasets covered by this document

Deliverable ID	Product title	Product type (CDR, ICDR)	Version number	Delivery date
WP2-FDDP-AER	IASI IMARS v7.1	CDR	V7.1	30/11/2023



Related documents

Reference ID	Document
RD1	E.U. Copernicus Climate Change Service (2024), C3S2_312a_D-WP2-FDDP-AER_202311_PUGS_v2.0: Product User Guide and Specification, http://wdc.dlr.de/C3S_312b_Lot2/Documentation/AER/C3S2_312a_Lot2_PUGS_AER_latest.pdf

Acronyms

Acronym	Definition
AAA	Asymptotic Approximation Approach for simulation of optical properties
ADT	Anomalous Defraction Theory
AERONET	Aerosol Robotic Network
AOD	Aerosol Optical Depth
ATBD	Algorithm Theoretical Basis Document
BTD	Brightness Temperature Difference
DLR	German Aerospace Center
DFD	German Remote Sensing Data Center
EPS	EUMETSAT Polar System
Eq.	Equation
ESA	European Space Agency
EUMETSAT	European Organization for the exploitation of Meteorological Satellites
Fig.	<i>Figure</i>
FLT32	32 Bit (4 Byte) floating point numbers
FORTRAN	FORmula TRANslation programming language
FOV	Field of View ("pixel")
IASI	Infrared Atmospheric Sounding Interferometer
IDL	Interactive Data Language
IMARS	Infrared Mineral Aerosol Retrieval Scheme
INT16	16 Bit (2 Byte) Integer numbers
L0	Data Level 0
L1	Data Level 1
L2	Data Level 2
L3	Data Level 3
L4	Data Level 4



LUT	Look-Up Table
METOP	Meteorological Operational satellite
NASA	National Aeronautics and Space Administration (USA)
netCDF / nc	Network Common Data Format
NOAA	National Oceanic and Atmospheric Administration (USA)
PCS	Principal Components Scores
PSUG	Product Specification and User Guide
SDA	Spectral Deconvolution Algorithm
SEVIRI	Spinning Enhanced Visible and InfraRed Imager
TIR	Terrestrial InfraRed spectrum
UTC	Universal Time Coordinate

General definitions (main aerosol variables)

- Climate Data Record (CDR)** A (Thematic) Climate Data Record is derived from a FCDR and closely connected to an ECV but strictly covers one geophysical variable, whereas an ECV can encompass several geophysical variables. A (F)CDR can encompass several instruments.
- Data Product (or: ECV product)** The geophysical product underlying a (I)CDR, characterized by product definition, product name, processing level, instruments used, processing algorithm (name and version), data provider, and data format.
- Essential Climate Variable (ECV)** A geophysical variable that is associated with climate variation and change as well as the impact of climate change onto Earth [GCOS-200]. ECVs might encompass a set of CDRs with associated Data Products.
- Fundamental Climate Data Record (FCDR)** A well-characterized, long-term data record of, *e.g.*, calibrated radiances, with calibrations sufficient to allow the generation of a Data Product that is accurate and stable, in both space and time, to support climate applications. A FCDR includes the ancillary data used in the calibration [GCOS-200].
- Interim Climate Data Record (ICDR)** A CDR which is regularly updated with an algorithm/system having maximum consistency to the CDR generation algorithm/system. The update cycle depends on the user requirements [GCOS-200].



Level 1	Measured satellite data product: geolocated radiance (spectra)
Level 1C	Measured satellite data product: geolocated radiance (spectra with radiometric and geometric corrections applied)
Level 2	Satellite-derived data product: geolocated geophysical variables. Here: O3, aerosol or CO ₂ and CH ₄ information for each ground-pixel
Level 3	Aggregated satellite data product: gridded geophysical variables Here: Gridded O3, aerosol or CO ₂ and CH ₄ information, e.g., 5 deg times 5 deg, monthly
Level 4	Satellite-derived data product: Here: Assimilated O3 columns or Surface fluxes (emission and/or uptake) of CO ₂ and CH ₄
Brokered dataset	Datasets, which are produced outside this contract and are then simply made accessible as part of this service
Sensor line	A series of sensors with similar instrument characteristics onboard subsequent satellite platforms with similar orbit characteristics – the data from all these sensors can be used to create a combined long-term ECV from the sensor line

List of variables used in equations

τ	Optical depth
ν	Frequency
μ	Cosine of viewing angle
I	Incident Radiation
ε	Retrieval uncertainty
T	Temperature
T_{sfc}	Surface temperature
T_{dust}	Dust layer temperature
B_{ν}	Planck function
ω_0	Single scattering albedo
P_s	Scattering phase function
g	Asymmetry parameter
$\mu \frac{dI(\tau, \nu, \mu)}{d\tau}$	Spectral radiative transfer equation



L_{\downarrow}	Downwelling spectral radiance
L_{\uparrow}	Upwelling spectral radiance
A_{sfc}	Surface albedo
T_{gas}	Atmospheric transmissivity due to gas absorption
A	Dust layer absorptivity, e.g. eq. (7)
R	Dust layer reflectivity, e.g. eq. (5)
T	Dust layer transmissivity, e.g. eq. (6)
DFS	Degrees of freedom for signal
λ	Eigenvalue
H	Information Entropy
BTD	Brightness temperature difference
Q_{ext}	Extinction efficiency
Q_{scat}	Scattering efficiency
a_n, b_n	Mie coefficients
m	Complex refractive index
α	Polarizability
x	Particle size parameter
Q_{abs}	Absorption efficiency
$P_{Rayleigh}$	Rayleigh phase function
θ	Scattering angle
ϕ	Incidence angle
R	Fresnel reflectance
J_0	Zero-order Bessel function
P	Gaussian probability function
R_{eff}	Effective radius
D_{mw}	Mean-weighted diameter
AOD	Aerosol optical depth
γ	Thermal infrared-to-visible spectrum ratio



Table of Contents

History of modifications	3
List of datasets covered by this document	5
Related documents	6
Acronyms	6
General definitions (main aerosol variables)	7
List of variables used in equations	8
Scope of the document	13
Executive summary	13
1 Instruments	15
1.1 Metop satellites	15
1.2 IASI instrument overview	16
2 Input data requirements	17
2.1 IASI L1C data	17
2.2 Auxiliary data	18
3 Algorithms	19
3.1 Scientific background	20
3.1.1 Infrared resonance bands of mineral dust	20
3.1.2 Radiative transfer modelling and spectral aggregation	20
3.1.3 Physico-chemical characteristics of desert dust	24
3.1.4 Optical properties of non-spherical desert dust particles	25
3.1.5 Theoretical considerations of the IMARS retrieval approach	32
3.2 Implementation	35
3.2.1 IMARS processing environment	35
3.2.2 Preparatory steps	37
3.2.3 Surface emissivity	37
3.2.4 Implementation of the core dust retrieval	37
3.2.5 Quality Flags	39
3.2.6 A posteriori cloud discrimination and approval of results	41
3.3 Retrieval examples	42
4 Algorithm output	43
4.1 Generic IMARS output	43
4.2 IMARS CCI / C3S specific output	44



4.3 Guidelines for product use: confidence levels 47

References 48

List of tables

Table 1: IASI spectral bands and covering spectral ranges	17
Table 2: Required auxiliary datasets for IMARS and corresponding currently used sources.....	18
Table 3: Effective radius for the 12 dust representations used in IMARS. Dust mineralogical compositions as from Table 5.	24
Table 4: mass weighted mean diameter for the 12 dust representations used in IMARS. Dust mineralogical compositions as from Table 5.....	25
Table 5: Typical desert dust compositional mixtures used in the IMARS retrieval. All relative mineral contributions are calculated by volume.	25
Table 6: Mineralogical components and refractive index sources. For all minerals the refractive indices from the respective two sources have been averaged.....	25
Table 7: Quality flag conditions in IMARS	40
Table 8: Quality flag decisions in IMARS	41
Table 9: Output datasets contained in the generic IMARS output.	43
Table 10: Dataset names and contained variables of the aerosol_cci IMARS output files.....	45
Table 11: Guidelines for application of different levels of quality filtering.....	47

List of figures

Figure 1: Design of Metop EPS satellites. © EUMETSAT	15
Figure 2: Schematic view of the IASI measurement principle and FOV alignment. © CNES.....	16
Figure 3: IASI specified and theoretical spectral resolution© CNES	17
Figure 4: Full spectral resolution (blue) and binned-maximum-brightness-temperature (red) spectra of the IASI instrument for cases with (bottom) and without (top) desert dust signal. The pristine cases (i.e. no dust signal) are depicted for low (top left) and high (top right) water vapor content while the dust cases show spectra over ocean (bottom left) and over desert (bottom right) in order to illustrate the impact of surface emissivity.....	22
Figure 5: Degrees of Freedom for Signal as a function of dust AOD and dust layer temperature (left) and the dust information spectrum in the atmospheric window region (right).	23
Figure 6: Extinction efficiency (top), single scattering albedo (middle) and asymmetry parameter (bottom) for quartz (left) and illite (right) as simulated with the AAA method (blue) and Lorenz-Mie theory (red) as well as corresponding laboratory measurements of the University of Iowa (black) in the terrestrial IR spectral region. The spectra and size distributions correspond to the measurements described in [Mogili et al., 2008].	30
Figure 7: Extinction efficiency spectra of kaolinite rich (top) and illite/ quartz rich (bottom) dust samples as simulated with the AAA method (blue) and Lorenz-Mie theory (black) as well as corresponding laboratory measurements of the University of Paris East (red) in the terrestrial IR window region. The figures correspond to dust extinction directly after injection into the atmospheric simulation chamber (left) and after 50 minutes residence time (right) and consequently to different size distributions as larger particles deposit faster (see [Klüser et al., 2016])......	31
Figure 8: Example of simulated brightness temperature differences for various TIR AODs. These simulations have been performed with the “Iowa Loess” mixture and the lognormal “Aerosol_cci” particle size distribution for ocean (left) and desert (right) surface emissivities and for near-surface dust (approx. 500m, top) and an elevated dust layer (approx. 5km, bottom).	32



Figure 9: Example of simulated brightness temperature differences for various TIR ice cloud optical depths. These simulations have been performed for ocean surface emissivities at a moderate cloud height of (approx. 5km, bottom). Brightness temperature differences have been simulated for ice cloud with an effective diameter of 40 μm with the parameterizations of *Yang et al. 2005* (top left), *Baum et al. 2013* (top right), and the AAA disk model (bottom left). For the latter also the impact of crystal size of the BTD is exemplarily presented for simulations with an effective radius of 80 μm 34

Figure 10: Overview of the IMARS processing environment..... 36

Figure 11: Program flow chart of the IMARS retrieval. The retrieval loop is repeated for all FOVs per scanline and for all scanlines of the granule/orbit. This flow chart is a close-up of the blue box in Figure 10..... 38

Figure 12: Modular design of the IMARS version 7.0 algorithm chain independently performed for each FOV. This module plot is a schematic close-up of the white box (“imars_loop”) in Figure 11. 39

Figure 13: IMARS v7.0 results for P_{dust} (top left) and P_{cloud} (top right) and H (bottom left) as well as dust $AOD_{0.55\mu\text{m}}$ (bottom right) for the large dust outbreak off the coast of West Africa on 17 September 2010 observed with IASI on board Metop-A. 42



Scope of the document

This document describes the theoretical basis for the mineral dust aerosol retrieval algorithm developed by DLR-DFD for the Infrared Atmospheric Sounding Interferometer (IASI) instruments on board of EUMETSAT's METOP satellites. It describes the algorithm, referenced as Infrared Mineral Aerosol Retrieval Scheme (IMARS), used to generate mineral dust and ice cloud products. It also includes the scientific justification for deriving said products, an outline of the proposed approach as well as a listing of assumptions and limitations of the algorithm.

The initial development of this algorithm and first improvement cycles were conducted under ESA Aerosol_cci projects, before it was handed over for routine processing to C3S under the contracts C3S_312a_Lot5 and currently C3S_312b_Lot2. Currently further algorithm development is conducted with internal funding of the provider.

This ATBD aims to provide an overview of the IMARS algorithm with detailed references, with summaries of the issues that are important for the Aerosol C3S work and specifically the IMARS retrieval scheme. It will not be a comprehensive compilation of all existing literature on the topic of hyperspectral infrared aerosol retrieval.

Executive summary

The IMARS scheme is based on probabilistic estimation of the atmospheric state with respect to desert dust and ice clouds, based on pseudo-channel simulations of the observed signal for various dust and ice cloud properties. The solution to the radiative transfer problem is approximated by a generalized Two-Stream approach for spectrally resolved infrared radiative transfer. It is inspired by previous approaches for hyperspectral dust remote sensing in the terrestrial infrared. A total of 6000 brightness temperature difference sets (each being built from three pseudo-channel brightness temperatures) have been simulated with varying dust particle size distributions, mineralogical compositions, infrared optical depths and layer heights. The same number of simulations has been performed for ice clouds. Based on a Gaussian distance metric the probability distribution function (PDF) over these 6000 instances is determined and the state vector as well as its probability and uncertainty are estimated from the PDF.

Optical properties have been obtained with the "Asymptotic Approximation Approach" (AAA) for non-spherical particles and have been evaluated with laboratory measurements of extinction spectra. Extinction and scattering efficiencies as well as asymmetry parameter and single scattering albedo have been pre-tabulated for each particle size distribution and mixture. Ice cloud optical properties have been compiled from a range of parameterizations found in the scientific literature as well as from the Asymptotic Approximation Approach for simulation of optical properties (AAA).

The retrieval approach is followed sequentially for dust and ice clouds. An a posteriori cloud screening is performed based on probability and uncertainty estimates determined within the probabilistic retrieval itself. IMARS output also includes pixel-wise uncertainty estimates for all optical-depth products as well as an early stage uncertainty, and also a retrieval entropy describing the average



information content conveyed by the calculated dust and cloud probabilities. Both the uncertainty and retrieval entropy serve as dust/cloud discriminants within the dust quality flagging, which is also included in IMARS output.

The IMARS retrieval can be performed regardless of solar illumination as the contribution of reflected solar radiation to the observed spectra is extremely small. Furthermore, guidelines for IMARS product use are presented for four levels of quality filtering. The highest level of confidence in the IMARS results can be summarized as “trust everything with quality flag >3 , dust probability >0.5 , retrieval entropy <0.9 and uncertainty $<40\%$ ”. If sample size is more critical than absolute accuracy, it is advisable to release the filtering to “trust everything with quality flag >3 and retrieval entropy <0.9 ”.

Scientific publications referred to within this document describe earlier algorithm versions and do not reflect the latest changes (including those within Aerosol_cci as an outcome of the project work) implemented into the scheme and documented within this ATBD. All references to IMARS within Aerosol CCI and C3S should thus include the citation of the latest issue of this ATBD.

Section 1 presents the instruments and satellites they are mounted on. Section 2 discusses the required input data needs. Section 3 lays out the scientific background and implementation from preparing to executing the retrieval. Section 4 lays out how retrieval output is structured and what is included.



1 Instruments

IMARS uses data sourced by the IASI instruments¹ onboard the European Metop satellites². IASI is a passive remote sensing device measuring in nadir view. The optical spectrum is predominantly sensitive to infrared and beyond wavelengths due to its passive nature and the solar-synchronous polar orbit of Metop following earth’s twilight zone.

1.1 Metop satellites

The European Polar System (EPS) consists of three Metop satellites with Metop-A in orbit since October 2006, Metop-B since 2012 and Metop-C since 2018. EPS is the European contribution to the Initial Joint Polar System (IJPS) agreed upon by EUMETSAT and NOAA. The European and American satellites of the IJPS carry a set of identical sensors: AVHRR/3, AMSU-A, HIRS/4 and MHS.

The European EPS satellites carry an additional set of sensors as well: IASI, ASCAT, GOME-2 and GRAS. Moreover they operate the Argos Advanced Data Collection System (A-DCS). The design of the Metop satellites is depicted in Figure 1. Equator crossing time of the EPS satellites is 09:30 local solar time at an altitude of 817km and an inclination of 98.7°.

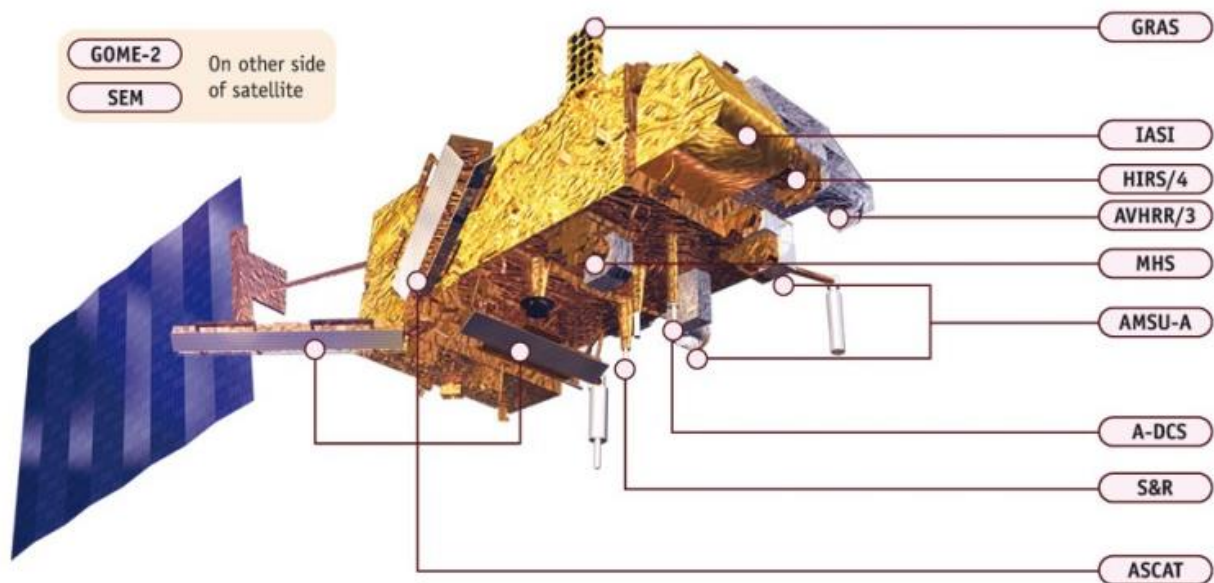


Figure 1: Design of Metop EPS satellites. © EUMETSAT

¹ <https://www.eumetsat.int/iasi>

² <http://www.eumetsat.int/website/home/Satellites/CurrentSatellites/Metop/index.html>

1.2 IASI instrument overview

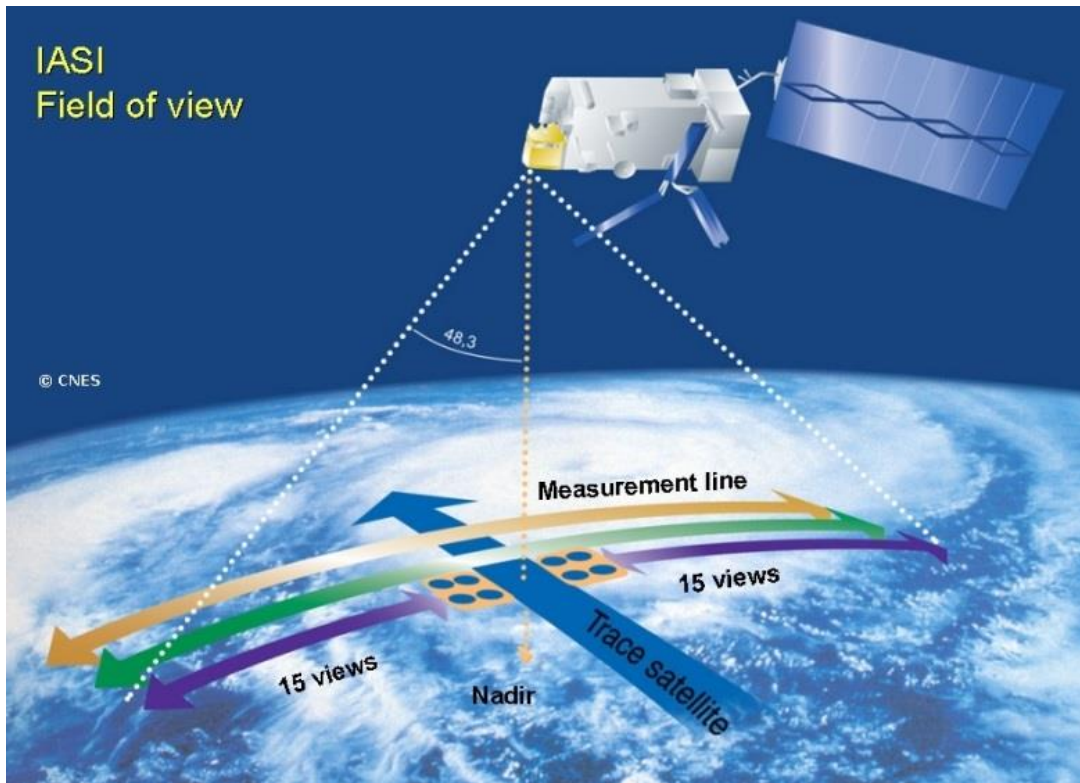


Figure 2: Schematic view of the IASI measurement principle and FOV alignment.
© CNES.

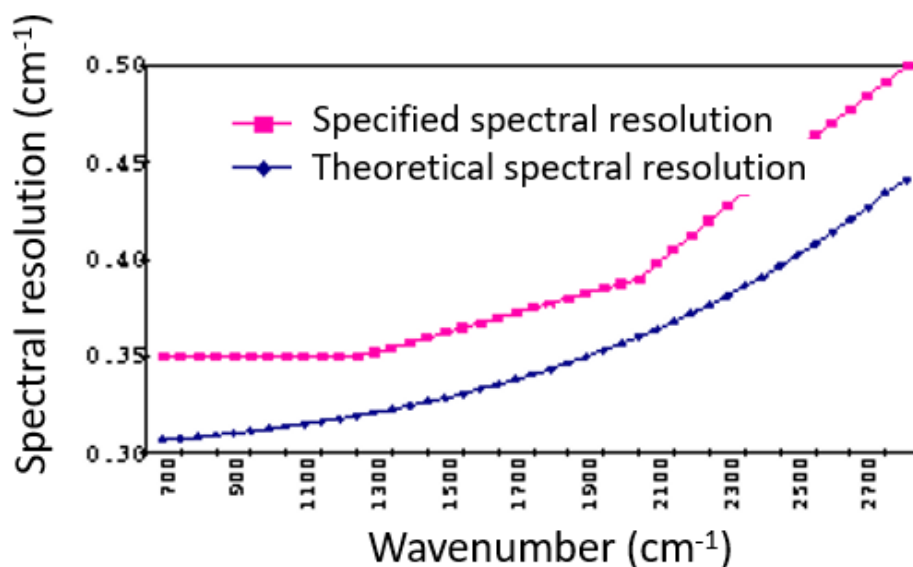
On board the Metop satellites is the Infrared Atmospheric Sounding Interferometer (IASI), a scanning Michelson interferometer with very fine spectral resolution in the terrestrial infrared designed for observation of atmospheric temperature and humidity profiles. It observes infrared radiance spectra in the range of $3.6\mu\text{m} - 15.5\mu\text{m}$ (in three overlapping bands, Table 1) at 12km nadir ground resolution and a swath of 48.3° (2200km). It scans the earth with four detectors simultaneously and each swath (scanline) is divided into 30 2×2 scan matrices, i.e. each scanline contains 60 fields-of-view (FOV). The scan principle is shown in Figure 2 schematically. The ground resolution of 12km is a tradeoff between radiometric performance and the statistical likelihood of valid measurement acquisition depending on cloud cover.

8461 channels in the terrestrial infrared result in a spectral resolution of less than 0.5cm^{-1} (Figure 3). Instrument stability is as high as 0.3K at an absolute accuracy of 0.5K. The spectral resolution of apodized L1C spectra is 0.5cm^{-1} over the entire spectrum.



Table 1: IASI spectral bands and covering spectral ranges

Band	Range (cm ⁻¹)	Range (μm)
1	645 to 1210	15.5 to 8.26
2	1210 to 2000	8.26 to 5
3	2000 to 2760	5 to 3.62

Figure 3: IASI specified and theoretical spectral resolution³© CNES

2 Input data requirements

2.1 IASI L1C data

The spectral input for IMARS is generated from IASI level 1C radiance files, which are acquired in the EUMETSAT native data format as full spectra (product code “_xxx_”, preferred version). Data have to be delivered with correct geolocation, viewing angle and observation time.

In order to facilitate the processing, IMARS is designed to build on preprocessed data of spectral input from earlier IMARS versions. As of IMARS v7.0 the preprocessor runs in python programming language, is independent of EUMETSAT’s reading routines, and supports a parallelization scheme like every other part of the processing chain. The minimum requirement for input data is spectrally binned brightness temperatures or radiances in the 833cm⁻¹ – 1250cm⁻¹ band as described earlier, at least containing the 35 bin values used for the retrieval (as specified in Table 9). The preprocessed data have to contain geolocation, viewing angles and observation time in the same array structure as the spectral input (Table 9). Consequently the input of IMARS v7.1 is not original EUMETSAT IASI L1C spectra but adjusted IMARS input files. Theoretically it is also possible to provide input from other

³ https://iasi.cnes.fr/en/IASI/spectral_res.htm



sensors, as long as they are able to provide the three brightness temperatures used in IMARS. Unfortunately for narrowband instruments the spectral binning aiming at minimizing the gas absorption impact (especially from water vapor) is not available so that the quality will necessarily be reduced from imager input data.

2.2 Auxiliary data

Auxiliary data include lookup tables for dust and ice clouds as will be needed in chapter 3. Moreover IMARS requires surface elevations. Currently the ETOPO-2 digital elevation model (DEM) is used for mapping surface elevation onto a global 0.1° latitude/longitude grid.

Table 2 shows the required auxiliary data input as currently implemented in IMARS together with the corresponding sources of the data; only the last instance of source is presented here. While these can themselves rely on auxiliary inputs, e.g. the refractive indices in the case of AAA simulations or the optical properties in the case of the Two-Stream simulations, these details can be found in preceding chapters of this document and, further, they are not essential for the IMARS algorithm. For example, the dust optical properties required by the algorithm are not bound to be derived with AAA simulations; other methods would also fit the purpose, e.g. T-Matrix for optical properties, or advanced radiative transfer modelling instead of the Two-Stream approximation for the lookup tables.

Table 2: Required auxiliary datasets for IMARS and corresponding currently used sources.

Auxiliary dataset	Dimensions	Source	Data format
Digital elevation model	7200x3600	ETOPO-2 on 0.1° lat/lon projection	netCDF-3
Dust R_{eff}	4x6	Table 3	netCDF-4
Dust D_{mw}	4x6	Table 4	netCDF-4
Dust composition matrix	4x6	Table 5	netCDF-4
Dust g (TIR)	3x4	AAA	netCDF-4
Dust ω_0 (TIR)	3x4	AAA	netCDF-4
Dust γ	3x4	AAA	netCDF-4
Dust Q_e (TIR)	3x4	AAA	netCDF-4
Dust BTD_1 LUT ocean surface	100x5x3x4	AAA/Two-Stream	netCDF-4
Dust BTD_2 LUT ocean surface	100x5x3x4	AAA/Two-Stream	netCDF-4
Dust BTD_3 LUT ocean surface	100x5x3x4	AAA/Two-Stream	netCDF-4
Dust BTD_4 LUT ocean surface	100x5x3x4	AAA/Two-Stream	netCDF-4
Dust BTD_1 LUT desert surface	100x5x3x4	AAA/Two-Stream	netCDF-4
Dust BTD_2 LUT desert surface	100x5x3x4	AAA/Two-Stream	netCDF-4
Dust BTD_3 LUT desert surface	100x5x3x4	AAA/Two-Stream	netCDF-4
Dust BTD_4 LUT desert surface	100x5x3x4	AAA/Two-Stream	netCDF-4
Cloud R_{eff}	4	Intrinsic	netCDF-4
Cloud g (TIR)	3x4	literature+AAA	netCDF-4
Cloud ω_0 (TIR)	3x4	literature+AAA	netCDF-4



Cloud γ	3x4	literature+AAA	netCDF-4
Cloud Q_e (TIR)	3x4	literature+AAA	netCDF-4
Cloud BTD_1 LUT ocean surface	100x5x3x4	literature+AAA/Two-Stream	netCDF-4
Cloud BTD_2 LUT ocean surface	100x5x3x4	literature+AAA/Two-Stream	netCDF-4
Cloud BTD_3 LUT ocean surface	100x5x3x4	literature+AAA/Two-Stream	netCDF-4
Cloud BTD_4 LUT ocean surface	100x5x3x4	literature+AAA/Two-Stream	netCDF-4
Cloud BTD_1 LUT desert surface	100x5x3x4	literature+AAA/Two-Stream	netCDF-4
Cloud BTD_2 LUT desert surface	100x5x3x4	literature+AAA/Two-Stream	netCDF-4
Cloud BTD_3 LUT desert surface	100x5x3x4	literature+AAA/Two-Stream	netCDF-4
Cloud BTD_4 LUT desert surface	100x5x3x4	literature+AAA/Two-Stream	netCDF-4
Altitude level radiance ratio	5	Intrinsic	netCDF-4
TIR simulation optical depth	100	Intrinsic	netCDF-4

3 Algorithms

This chapter summarizes the main physical principles underlying the IMARS algorithm and its implementation.

Mineral dust in the atmosphere has gained increased scientific interest in recent years owing to its important role in the climate system and its impacts on air quality. Airborne dust interacts directly with solar and terrestrial radiation. Dust particles can also act as cloud condensation nuclei or ice nuclei, altering cloud microphysical and optical properties. Both direct and indirect effects alter the radiation balance, and thus atmospheric and surface heating. Dust from the Sahara, the largest dust source in the world, also acts as an important source of iron for maritime biogeochemistry (e.g. [Mahowald et al., 2010]).

In the terrestrial infrared (TIR) it is possible to detect a couple of aerosol types (e.g. [Clarisse et al., 2013]). The detectable aerosol types with highest atmospheric abundance and mass load together with the highest impacts on environment and climate are desert dust and volcanic ash. They are generally well detectable in TIR due to Si-O and other resonance bands which dramatically increase absorption and scattering in the TIR. Moreover particle sizes of dust and volcanic ash are sufficiently large for resulting in sufficiently high volume extinction, so that the signal can be extracted from TIR observations.

The IMARS algorithm provides an estimate of the dust AOD (aerosol optical depth) in TIR as well as an estimate of the visible dust AOD based on the retrieved dust particle size and composition. Moreover mass columns and dust layer effective emission temperature are retrieved alongside. The IMARS data can be used to assess the atmospheric dust load as well as to function as prior or posterior estimate of the aerosol type for other retrieval algorithms.

Aerosol retrievals in TIR dust remote sensing face different challenges than those using solar wavelengths. The radiation source is the earth's surface as well as the atmosphere itself. Contributions of (reflected) solar radiation to the TIR radiance observed from space is extremely small. Consequently atmospheric profiles play a crucial role in determining the radiance observed by TIR satellite instruments. The surface leaving radiance is additionally governed by the surface



emissivity, which over sparsely vegetated land areas causes significant problems. Also the absorption (and consequently also emission) by gases, mainly water vapor and ozone, further complicate the retrieval. Additionally, dust itself shows a large variability in optical properties depending on particle size, particle shape and dust composition. All these determine the absorption and scattering properties as well as the thermal emission of dust. Exact treatment of all these strongly varying parameters would cause immense computational costs for any retrieval algorithm, thus any TIR dust retrieval algorithm has to make (partly critical) assumptions and simplifications.

3.1 Scientific background

3.1.1 Infrared resonance bands of mineral dust

The majority of airborne mineral dust is composed of silicate minerals like quartz or silicate clays. Moreover carbonates and sulfates as well as iron oxides are commonly found in mineral dust samples (e.g. [Caquineau et al., 1998], [Formenti et al., 2008] and-[Kandler et al., 2011]).

Silicates are characterised by strong $\nu(Si-O)$ vibrational stretch resonance bands around 1050cm^{-1} [$9.5\mu\text{m}$]. Layered aluminosilicates like kaolinite also show a significant secondary $\delta(Al-Al-OH)$ vibrational resonance band around 920cm^{-1} (see e.g. [Clarisse et al., 2013]).

Although maximum extinction of TIR radiation by silicates is observed around 1050cm^{-1} [$9.5\mu\text{m}$], the peak extinction is masked by the strong O_3 absorption band around 1040cm^{-1} [$9.6\mu\text{m}$]. But as the broad silicate resonance band shoulders stretch to outside the O_3 absorption band, the extinction signal still can be detected from space-borne TIR observations (e.g.[Ackermann, 1997]).

The iron oxides hematite and limonite/goethite exhibit a weak resonance band at 1025cm^{-1} which is only 2% of the intensity of $Si-O$ resonance in this region. Thus the iron oxide absorption is generally masked by silicate peaks in airborne dust and cannot be detected from TIR satellite observations ([Sokolik and Toon, 1999]).

As a consequence spectral characteristics of dust extinction have to be known or assumed for extracting quantitative dust information from TIR instruments. The strong impact of variable assumptions about dust infrared optical properties on retrieval results from IASI has been shown in [Kluser et al., 2015].

3.1.2 Radiative transfer modelling and spectral aggregation

The azimuthally averaged form of the spectral radiative transfer equation for thermal infrared radiation including scattering as formulated e.g. in [Ackermann, 1997] is

$$\mu \frac{dI(\tau, \nu, \mu)}{d\tau} = I(\tau, \nu, \mu) - (1 - \omega_0(\nu)) \cdot B_\nu(T(\tau)) - \left(\frac{\omega_0(\nu)}{2}\right) \cdot \int_0^\mu P_s(\tau, \nu, \mu, \mu') \cdot I(\tau, \nu, \mu') d\mu', \quad (1)$$

where μ is the cosine of the viewing angle, τ is optical depth, $I(\tau, \nu, \mu)$ is the incident radiation, $B_\nu(T)$ represents the Planck function for given temperature T , ω_0 is the single scattering albedo defined by β_{scat}/β_{ext} (with $\beta_{ext} = \beta_{scat} + \beta_{abs}$) and P_s is the scattering phase function.



By knowing the spectrally resolved optical depth $\tau(\nu)$, the single scattering albedo $\omega_0(\nu)$ and the asymmetry parameter $g(\nu)$, we can simulate the effective transmissivity of dust with a discrete-ordinates approximation, specifically the Two-Stream solution of the radiative transfer equation including atmospheric scattering (Eq. (1)), but neglecting multiple scattering effects between the surface and the dust layer.

Using L_{\downarrow} , the downwelling spectral radiance at the top-of-atmosphere (negligible in TIR) and $L_{\uparrow} = \varepsilon_{sfc} B_{\nu}(T_{sfc})$ with surface temperature T_{sfc} , the upwelling spectral radiance at the surface, as boundary conditions and furthermore assume isotropic emission by the surface and the dust layer (assumed isothermal with temperature T_{dust}), the Two-Stream solution of the radiative transfer problem can be formulated as ([Petty, 2006])

$$I_{sat}(\nu) = \left(R(\nu) + \frac{A_{sfc}(\nu) T_{gas}(\nu) T(\nu)^2}{1 - A_{sfc}(\nu) R(\nu)} \right) L_{\downarrow}(\nu) + \frac{T_{gas}(\nu) T}{1 - A_{sfc}(\nu) R(\nu)} L_{\uparrow}(\nu) + T_{gas}(\nu) A(\nu) \cdot B_{\nu}(T_{dust}). \quad (2)$$

In this formulation A_{sfc} is the surface albedo (which equals to $1 - \varepsilon_{sfc}$ according to Kirchhoff's law, assuming the transmissivity of solid earth to be zero), T_{gas} is the atmospheric transmissivity due to gas absorption, A is the absorptivity of the dust layer, R is the reflectivity of the dust layer and T is the transmissivity of the dust layer. The latter three quantities are calculated using

$$\Gamma(\nu) = 2\sqrt{1 - \omega_0(\nu)}\sqrt{1 - g(\nu)\omega_0(\nu)} \quad (3)$$

and

$$R_{\infty}(\nu) = \frac{\sqrt{1 - g(\nu)\omega_0(\nu)} - \sqrt{1 - \omega_0(\nu)}}{\sqrt{1 - g(\nu)\omega_0(\nu)} + \sqrt{1 - \omega_0(\nu)}} \quad (4)$$

as follows

$$R(\nu) = R_{\infty}(\nu) \frac{e^{\Gamma(\nu)\tau(\nu)} - e^{-\Gamma(\nu)\tau(\nu)}}{e^{\Gamma(\nu)\tau(\nu)} - R_{\infty}(\nu)^2 e^{-\Gamma(\nu)\tau(\nu)}} \quad (5)$$

$$T(\nu) = \frac{1 - R_{\infty}(\nu)^2}{e^{\Gamma(\nu)\tau(\nu)} - R_{\infty}(\nu)^2 e^{-\Gamma(\nu)\tau(\nu)}} \quad (6)$$

$$A(\nu) = 1 - R(\nu) - T(\nu), \quad (7)$$

where $\tau(\nu)$ is the dust AOD intended to be retrieved by IMARS. It is clearly evident, that Eq. (1) cannot simply be inverted and solved for $\tau(\nu)$. The IMARS scheme exploits IASI radiances in the atmospheric window in the 8-12 μm domain (825 cm^{-1} -1250 cm^{-1}).

In order to avoid contamination by narrow gas absorption lines the radiances are collected into bins of 10 IASI channels each; thus from 420 channels between 833 cm^{-1} and 1250 cm^{-1} 42 spectral bins are derived. Then the channel with the highest brightness temperature per bin is assumed to be affected the least by the atmospheric state. This assumption works fine for small single absorption lines but becomes rather questionable at the edge of the water vapor continuum (see Figure 4). Consequently in moist conditions the uncertainty of the dust signal increases. 7 bins are highly contaminated by strong O₃ absorption and are not used, resulting in 35 spectral bins used in the dust retrievals ([Kl user



et al., 2012]). Figure 4 illustrates the maximum brightness temperature binning and the selection of spectral bins around the O₃ absorption band.

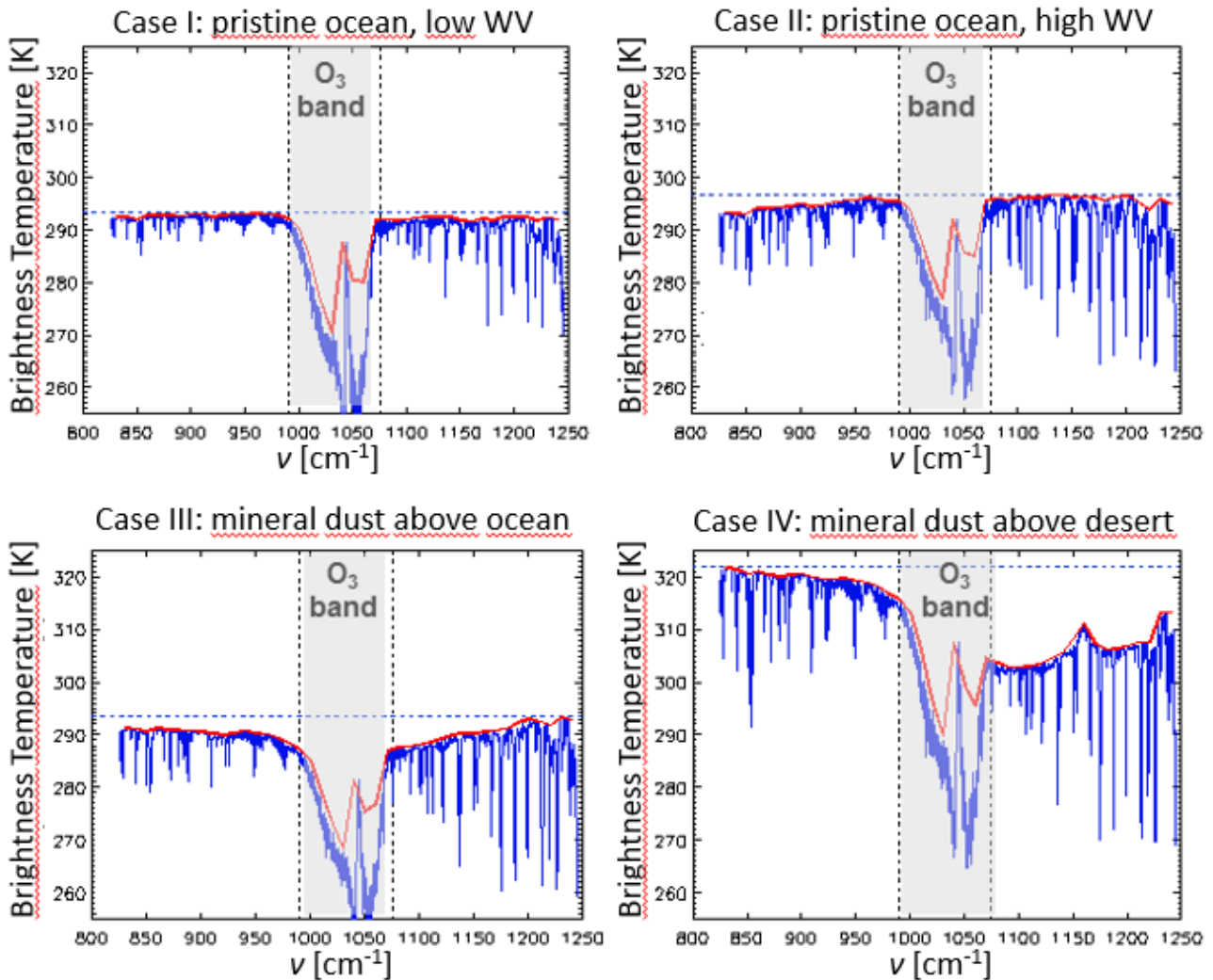


Figure 4: Full spectral resolution (blue) and binned-maximum-brightness-temperature (red) spectra of the IASI instrument for cases with (bottom) and without (top) desert dust signal. The pristine cases (i.e. no dust signal) are depicted for low (top left) and high (top right) water vapor content while the dust cases show spectra over ocean (bottom left) and over desert (bottom right) in order to illustrate the impact of surface emissivity.

Information content analysis of these spectra simulated with different sets of optical dust properties shows a maximum of more than 5 degrees of freedom for signal (DFS) and a mean of around 3 to 4 (Fig. 5).

The degrees of freedom for the signal are calculated using the eigenvalues λ of the covariance matrix of the spectrum as ([Rodgers, 2000])



$$DFS = \sum_i \frac{\lambda_i^2}{1+\lambda_i^2} \tag{8}$$

The information content is not equally distributed over the spectrum, but it is highest near the Si-O resonance peak and drops significantly towards the outward boundaries of the window region (Figure 5). The information spectrum ([Klüser et al., 2015], [Rodgers, 2000]) is based on the *information content* or information entropy H ([Shannon, 1949], [Shannon and Weaver, 1949]) and is evaluated for all spectral bins j as the sum over the histogram p (realized with 50 bins) of the brightness temperature values for the respective bin. Brightness temperature spectra have been simulated for a wide range of dust properties (composition and size distribution), dust AOD and dust layer height (see subsequent chapters for details).

$$\forall j \in [1,35]: H(j) = - \sum_{i=1}^{50} p_i(T_i[j]) \cdot \log_2(p_i(T_i[j])) \tag{9}$$

The information content analysis reveals a high redundancy among the 35 spectral bins. Consequently IMARS processing time can be decreased by subselection or aggregation into 3-6 information channels. Channel selection is partly based on the information spectrum (Figure 5) and partly on considerations of potential wider application possibilities for IMARS.

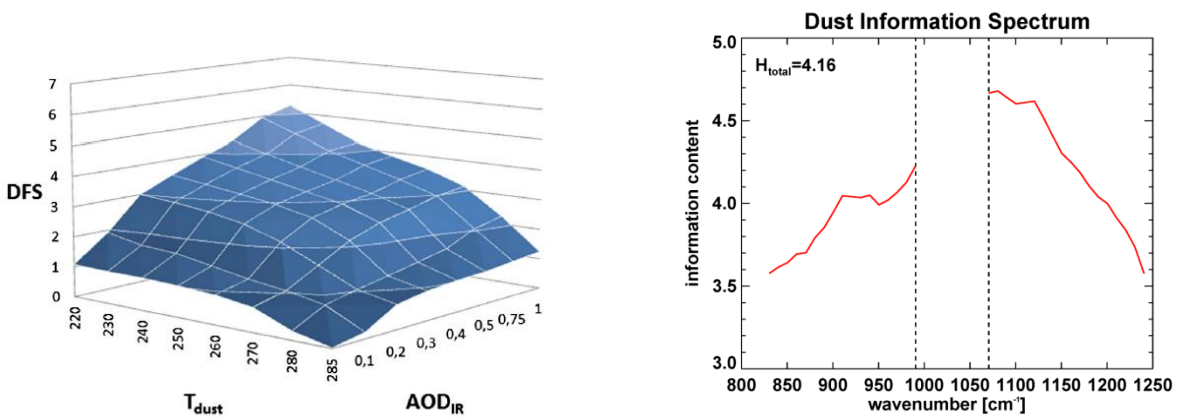


Figure 5: Degrees of Freedom for Signal as a function of dust AOD and dust layer temperature (left) and the dust information spectrum in the atmospheric window region (right).

Consequently, from IMARS v7.0, 28 out of 35 bins are aggregated into three pseudo-channels mimicking the three TIR window channels of narrow-band imaging instruments such as the *Spinning Enhanced Visible and InfraRed Imager* (SEVIRI) on board of the Meteosat Second Generation satellites or the *MODerate resolution Imaging Spectro-radiometer* (MODIS) on the US Earth Observation Satellites (EOS) “Aqua” and “Terra”. The aggregation is performed by collecting 14 bins (with minimized gas absorption signal) into one pseudo-channel centered at 1149.5cm⁻¹ (8.7µm) and reflecting a channel band width of 0.8 µm. Furthermore, 10 bins are collected into a pseudo-channel centered at 926.0cm⁻¹ (10.8µm, channel width of 1.0 µm) and 4 bins at the lower end of the wavenumber spectrum represent a pseudo-channel of 0.5µm width centered at 840cm⁻¹ (11.9µm). For simplicity, the brightness temperatures of these three pseudo-channels are referred to as T_{08} , T_{11} and T_{12} in the remainder of this document.



The baseline temperature is calculated as the maximum of the three pseudo-channel brightness temperatures

$$T_{base} = \max\{T_{08}, T_{11}, T_{12}\}. \quad (10)$$

The three pseudo-channel brightness temperatures are collected into a set of four brightness temperature differences reflecting the spectral variation of the dust (or cloud or surface) signal:

$$BTD_1 = T_{08} - 2T_{11} + T_{12}, \quad (11)$$

$$BTD_2 = T_{11} - T_{12}, \quad (12)$$

$$BTD_3 = T_{08} - T_{12}, \quad (13)$$

$$BTD_4 = T_{08} - T_{11}. \quad (14)$$

3.1.3 Physico-chemical characteristics of desert dust

The very high variability in particle size, particle shape and mineralogical composition of aeolian dust has strong consequences for infrared optical properties (e.g. [Sokolik and Toon, 1999], [Yang et al., 2007]). From IMARS v7.0, three different size distributions and four representative mineralogical dust mixtures are used. The size distributions represent the mono-modal dust particle size distribution used in the solar algorithms of Aerosol_cci ([De Leeuw et al., 2015]), as well as two size distributions describing the dust samples used for atmospheric simulation chamber measurements ([Mogili et al., 2008], [Di Biagio et al., 2014], [Klüser et al., 2016]). The latter describe one size distribution of dust sampled in an active dust source region (“China1” from [Klüser et al., 2016], described in detail in [Di Biagio et al., 2014]) dominated by rather coarse particles and one size distribution determined from the individual contributions of dust components as described in [Mogili et al., 2008]. Consequently both size distributions representing laboratory measurements account for domination of different particle modes by different mineralogical components of the dust. Moreover, as the absorption spectra samples by the University of Iowa (referred to as “Iowa” size distribution in the following) have been acquired for single mineral samples with individual size distributions, the resulting size distribution of the “Iowa” class is different for each mineralogical mixture ([Klüser et al., 2016]). The combination of four mixtures and three size distributions yields a set of 12 dust representations with different size distributions. Table 3 lists the corresponding effective radii, Table 4 the corresponding mass-weighted mean diameter D_{mw} (see e.g. [Mogili et al., 2008], [Klüser et al., 2016]) and Table 5 the mineralogical compositions of the three dust mixtures used in IMARS. The contribution of iron oxides and other heavy minerals has not been accounted for as the impact on TIR spectra is usually negligible and thus no information about these can be reliably obtained from TIR observations.

Table 3: Effective radius for the 12 dust representations used in IMARS. Dust mineralogical compositions as from Table 5.

	China	Central Sahara	Niger	Iowa Loess
Aerosol_cci	1.93 μm	1.93 μm	1.93 μm	1.93 μm
LISA	2.76 μm	2.76 μm	2.76 μm	2.76 μm
Iowa	1.33 μm	1.45 μm	0.76 μm	1.96 μm



Table 4: mass weighted mean diameter for the 12 dust representations used in IMARS. Dust mineralogical compositions as from Table 5.

	China	Central Sahara	Niger	Iowa Loess
Aerosol_cci	5.53 μm	5.53 μm	5.53 μm	5.53 μm
LISA	7.63 μm	7.63 μm	7.63 μm	7.63 μm
Iowa	7.77 μm	7.51 μm	5.18 μm	10.09 μm

Table 5: Typical desert dust compositional mixtures used in the IMARS retrieval. All relative mineral contributions are calculated by volume.

mixture	Ref.	quartz	illite	kaolinite	montm.	feldsp.	calcite
China	[Di Biagio et al., 2014]	21.6%	28.5%	8.5%	14.2%	0.0%	27.7%
C. Sahara	[Laskina et al., 2012]	1.4%	31.3%	16.2%	33.6%	8.8%	8.7%
Niger	[Di Biagio et al., 2014]	27.2%	6.9%	64.4%	0.0%	0.0%	1.5%
Iowa Loess	[Laskina et al., 2012]	0.0%	17.9%	0.0%	69.8%	11.4%	0.9%

3.1.4 Optical properties of non-spherical desert dust particles

Table 6 lists refractive indices used for the mineralogical components in the generation of infrared optical properties. In the case of birefringent minerals (quartz and calcite) a ratio of 2:1 for the ordinary and extraordinary rays is used (e.g. [Spitzer and Kleinmann, 1961]) for averaging the optical constants before the calculation of the optical properties.

Table 6: Mineralogical components and refractive index sources. For all minerals the refractive indices from the respective two sources have been averaged.

Component	Abbreviation	Refractive index reference
Quartz	Qz	[Spitzer and Kleinman, 1961] [Wenrich and Christensen, 1996]
Illite	Il	[Glotch et al., 2007] [Querry, 1987]
Kaolinite	Ka	[Querry, 1987] [Roush et al., 1991]
Montmorillonite	Mo	[Querry, 1987] [Roush et al., 1991]
Calcite	Ca	[Lane, 1999] [Long et al., 1993]
Feldspars	Fs	[Aronson et al., 1979] [Aronson, 1986]



Several studies analyzed the usefulness of Lorenz-Mie theory for estimation of dust optical properties in the TIR (e.g. [Klüser et al., 2015], [Klüser et al., 2012], [Yang et al., 2007], [Yang et al., 2005]) with dramatically differing results. Lorenz-Mie solutions for light scattering spheres consist of calculating extinction and scattering efficiencies Q_{ext} and Q_{scat} , respectively, by

$$Q_{ext} = \frac{2}{x^2} \sum_{n=1}^{\infty} (2n+1) \operatorname{Re}(a_n + b_n), \quad (15)$$

$$Q_{scat} = \frac{2}{x^2} \sum_{n=1}^{\infty} (2n+1) (|a_n|^2 + |b_n|^2). \quad (16)$$

The Mie coefficients (a_n and b_n) depend on the complex refractive index m as well as on the size parameter $x=2\pi r/\lambda$ (r stands for particle radius and λ for the wavelength of the incident light) and are thus spectral quantities. Especially for small particles the numerical solutions of Mie solvers become unstable ([Lentz, 1976], [Deirmendjian, 1969]). Moreover the effects of non-sphericity result in additional non-negligible uncertainty (e.g. [Klüser et al., 2015], [Mogili et al., 2008], [Legrand et al., 2014]).

A method for determining optical properties of non-spherical particles with arbitrary size distribution is the asymptotic combination of Rayleigh limit (i.e. small particles) solutions with geometric optics (i.e. large particles) solutions. This approach, termed “Asymptotic Approximation Approach” (AAA) has been described and evaluated in full detail in [Klüser et al., 2016]. Its basic theoretical foundations are outlined in this section.

For particles in the Rayleigh limit ($x \ll 1$) scattering can widely be neglected and the extinction efficiency is resembled by the particle absorption only. For non-spherical particles different approximations of Rayleigh limit absorptions have been formulated ([Mogili et al., 2008], [Hudson et al., 2008a], [Hudson et al., 2008b], [Bohren and Huffman, 1983]).

Absorption and scattering efficiencies in the Rayleigh limit can be described by the polarizability α ([Bohren and Huffman, 1983]):

$$Q_{abs,\alpha} = \frac{4}{3} x \operatorname{Im}(\alpha), \quad (17)$$

$$Q_{scat,\alpha} = \frac{16}{162} x^4 |\alpha|^2. \quad (18)$$

For the optical properties of non-spherical particles the radius r in x is the one of a volume equivalent sphere of the respective particle.

Regarding desert dust particles we mainly interested in the solutions derived using the “Continuous Distribution of Ellipsoids” (CDE) and the “Disk” approximations ([Hudson et al., 2008a], [Hudson et al., 2008b], [Mogili et al., 2008], [Bohren and Huffman, 1983]). The respective absorption efficiencies are then

$$Q_{abs,CDE} = \frac{4}{3} x \operatorname{Im} \left(\frac{2m^2}{m^2-1} \log[m^2] \right), \quad (19)$$

$$Q_{abs,disk} = \frac{4}{9} x \left(\frac{1}{(\operatorname{Re}[m^2])^2 + (\operatorname{Im}[m^2])^2} + 2 \right) \operatorname{Im}[m^2]. \quad (20)$$

The solutions are formally valid approximation only for $x \ll 1$ (in the Rayleigh limit). The corresponding scattering efficiencies for small ellipsoidal particles can be calculated by



$$Q_{scat,CDE} = \frac{16}{162} x^4 \left| \frac{2m^2 \log(m^2)}{m^2 - 1} \right|^2, \quad (21)$$

$$Q_{scat,disk} = \frac{16}{162} x^4 |m^2 - 1|^2 \left(\frac{1}{(\text{Re}[m^2])^2 + (\text{Im}[m^2])^2} + 2 \right). \quad (22)$$

Similar Rayleigh-limit solutions for the absorption and scattering efficiencies can also be derived for needle-shaped and spherical particles ([Bohren and Huffman, 1983]).

The scattering phase function in the Rayleigh limit is represented by the Rayleigh phase function

$$P_{Rayleigh}(\cos \theta) = \frac{3}{4} (1 + \cos^2 \theta). \quad (23)$$

The asymmetry parameter

$$g = \int_{-1}^1 P(\cos(\theta)) \cos(\theta) d \cos(\theta) \quad (24)$$

is zero in the Rayleigh limit as this is the analytical solution from the Rayleigh phase function. Moreover in the Rayleigh limit the scattering efficiency, being a function of x^4 , is typically very small, thus the Rayleigh limit contribution to anisotropic scattering is extremely small.

In the large particle limit the Mie solutions show an asymptotic behavior and tend to approximate an analytic solution (e.g. [Chýlek, 1975], [Acquista et al., 2980]). The asymptotic limit for Mie scattering of large spherical particles is

$$Q_{scat,lim} = 1 + \left| \frac{m-1}{m+1} \right|^2. \quad (25)$$

In the large particle limit the curvature radius of the sphere approaches infinity. Thus in the large particle limit all spheres can also be interpreted by Fresnel reflection on flat surfaces (which have curvature radius of infinity). The asymptotic Mie limit presented by [Acquista et al., 2980] shows that $Q_{ext,lim}=2$ regardless of absorption and thus fails to reproduce strong absorption bands. This approximation cannot reliably reproduce the optical properties of particles with strongly absorbing Reststrahlen bands (e.g. silicate).

For any incidence angle ϕ , the complex angle of refraction is defined by ([Bohren and Huffman, 1983])

$$\cos(\varphi') = \frac{\cos(\phi)}{m}. \quad (26)$$

and the Fresnel reflection coefficients are

$$r_1(\phi) = \frac{\sin(\phi) - m \cdot \sin(\phi')}{\sin(\phi) + m \cdot \sin(\phi')}, \quad (27)$$

$$r_2(\phi) = \frac{m \cdot \sin(\phi) - \sin(\phi')}{m \cdot \sin(\phi) + \sin(\phi')}. \quad (28)$$

The Fresnel reflectance of a large particle (i.e. x approaches infinity) follows from Eq. (27) and Eq. (28) as

$$R(\phi) = \frac{1}{2} (|r_1(\phi)|^2 + |r_2(\phi)|^2). \quad (29)$$

The transmission of an infinitely large particle becomes zero and the scattering efficiency can then be expressed by the angular integral over the Fresnel reflection ([v.d. Hulst, 1980]):

$$Q_{scat,Fresnel} = 1 + 2 \int_0^{\pi/2} R(\phi) \sin \phi \cos \phi d\phi, \quad (30)$$

where the first summand is the diffraction efficiency and the second summand (the integral) describes the reflection at the (particle) surface. In the limiting case of perpendicular incidence the Fresnel reflection approach is equal to the asymptotic Mie solution for large particles.

The Fresnel transmittance can likewise be calculated from

$$t_1(\phi) = \frac{2 \sin(\phi)}{\sin(\phi) + m \cdot \sin(\phi')}, \quad (31)$$



$$t_2(\varphi) = \frac{2 \sin(\varphi)}{m \cdot \sin(\varphi) + \sin(\varphi')}, \quad (32)$$

as

$$T(\varphi) = \frac{1}{2} (|t_1(\varphi)|^2 + |t_2(\varphi)|^2). \quad (33)$$

The Fresnell solution is used to calculate the path of individual rays at the particle surfaces for large particles. The extinction and absorption efficiencies of optically soft particles (i.e. diffraction not accounting for strong reflection at the particle surface) can also be estimated with the ADT ([v.d. Hulst, 1980], [Chýlek and Klett, 1991], [Maslowska, Flatau and Stephens, 1994]):

$$Q_{ext,ADT} = 4 \operatorname{Re} \left(\frac{1}{2} - \frac{\exp(-2xi \cdot (m-1))}{2x \cdot (m-1)} + \frac{\exp(-2xi \cdot (m-1)) - 1}{(2x \cdot (m-1))^2} \right), \quad (34)$$

$$Q_{abs,ADT} = 1 - 2 \frac{\exp(-4x \cdot \operatorname{Im}(m))}{4x \cdot \operatorname{Im}(m)} + 2 \frac{\exp(-4x \cdot \operatorname{Im}(m)) - 1}{(4x \cdot \operatorname{Im}(m))^2}. \quad (35)$$

The scattering efficiency is not directly determined with the ADT, but results from the difference between extinction and absorption. The approach is equivalent to the estimation of the absorption from the Lorenz-Mie solutions. The main advantage of using the ADT solution is that Q_{ext} and Q_{abs} can be estimated without assumptions about the particle shape. Strictly speaking ADT is only valid for particles with $|m/x - 1| \approx 0$ (optically soft particles), but that constraint mainly relates to the phase lag of the electromagnetic wave inside the particle and thus for the scattered (diffracted) ray. [Chýlek and Klett, 1991] nevertheless argue that the errors introduced by deviations from this conditions decrease significantly with increasing absorption. Consequently, it can be assumed that they are of minor importance near strong resonance absorption bands like those of silicate dust in the TIR.

As ADT mainly considers the diffraction of the light and does not reliably account for reflection at the particle surface, the scattering efficiency for large particles, including diffraction and reflection, can be approximated by combining Eq. (27), Eq. (28) and Eq. (29) and substituting the diffraction term in Eq. (30) by the corresponding ADT solution:

$$Q_{scat,A+F} = (Q_{ext,ADT} - Q_{abs,ADT}) + \int_0^{\pi/2} R(\varphi) \sin \varphi \cos \varphi d\varphi. \quad (36)$$

The scattering phase function for the large particle approximation can be calculated from combining Eq. (23), Eq. (29) and the angular diffraction pattern ([Bohren and Huffman, 1983]). The diffraction contribution is calculated as ([v.d. Hulst, 1980])

$$P_{diff}(\theta) = (1 - e^{-i\rho \sin \varphi}) \cdot J_0(x\theta \cos \varphi) \cdot \sin \varphi \cdot \cos \varphi. \quad (37)$$

where J_0 is the zero-order Bessel function, φ is the incidence angle as before and the scattering angle θ for the transmitted ray holds

$$\theta = 2(\varphi - \varphi'). \quad (38)$$

The combined phase function for the asymptotic large particle approximation then becomes

$$P_{A+F}(\theta) = P_{diff}(\theta) + R(\varphi, \varphi') + T(\varphi, \varphi') + (1 - R(\varphi, \varphi')^2) \cdot T(\varphi, \varphi')^2, \quad (39)$$



where ϕ and ϕ' determine the scattering angle θ according to the number of external and internal reflections.

A generalized solution for extinction and absorption by non-spherical particles is derived from combining the asymptotic Rayleigh and large particle approximations described earlier. While in the Rayleigh approximations the absorption efficiency is directly linear in x (Eq. (20) and (21)), in the large particle limit the Fresnel solutions for extinction, scattering and absorption efficiencies are functions of m and the incidence angle only while the ADT solutions show a more complex dependence on x , but no angular dependence. One way to combine the different solutions without strictly separating by size parameter thresholds is to use a weighting function which is nonlinear in x , bound to $[0,1]$ and asymptotically approaches 0 for small x and 1 for large x . This can be achieved by weighting of the two asymptotic solutions with an exponential decay function in the form

$$\begin{bmatrix} f_1 \\ f_2 \end{bmatrix} = \begin{bmatrix} 1 - e^{-y} \\ e^{-y} \end{bmatrix}. \quad (40)$$

Acknowledging that the validity of the Rayleigh approximation generally requires $x \ll 1$ while the validity of the geometric optics solution generally requires $x \gg 1$, there is good reasoning for postulating that both approaches shall be exactly equally weighted at $x=1$. The equality $f_1(y_0) = f_2(y_0)$ is valid exactly at $y_0 = -\ln(0.5)$. Thus we have

$$y = -x \cdot \ln\left(\frac{1}{2}\right) = x \cdot \ln(2) \quad (41)$$

in Eq. (40). Strictly speaking the Rayleigh approaches are valid only for $x \ll 1$, while the error of the Fresnel + ADT solution decreases as x approaches infinity. Thus both methods are good representations of the asymptotic behavior of extinction spectra in the small and large particle limits. Combining the Rayleigh and Fresnel + ADT solutions by f_1 respective f_2 yields the ‘‘Asymptotic Approximation Approach’’ (AAA) for arbitrary refractive index and particle size:

$$Q_{abs}(m, x) = f_1(x) \cdot Q_{abs,ADT}(m, x) + f_2(x) \cdot Q_{abs,Rayleigh}(m, x), \quad (42)$$

$$Q_{scat}(m, x) = f_1(x) \cdot Q_{scat,A+F}(m, x) + f_2(x) \cdot Q_{scat,Rayleigh}(m, x). \quad (43)$$

The Rayleigh limit method to be used (CDE or disk) depends on the mineral component (see [Klüser et al., 2012], [Mogili et al., 2008]). Extinction efficiency and single scattering albedo are obtained from $Q_{ext} = Q_{scat} + Q_{abs}$ and $\omega_0 = Q_{scat}/Q_{ext}$, respectively

The scattering phase function is calculated by

$$P(\theta) = \frac{e^{-x \ln(2)} \cdot Q_{scat,Rayleigh} \cdot P_{Rayleigh}(\theta) + (1 - e^{-x \ln(2)}) \cdot Q_{scat,A+F} \cdot P_{A+F}(\theta)}{Q_{scat,Rayleigh} + Q_{scat,A+F}}, \quad (44)$$

where the m - and x dependences are omitted for the sake of readability.

In a comparison study with laboratory extinction measurements of dispersed mineral dust ([Klüser et al., 2016]) the AAA method for calculating the optical properties of non-spherical particles of arbitrary size has shown very good agreement with the measurements.



Examples for dust extinction spectra calculated with traditional Mie theory, with the AAA method and the corresponding laboratory measurements (all from [Klüser et al., 2016]) are shown for quartz and illite in Figure 6. Also the corresponding spectra of single scattering albedo and asymmetry parameter are shown.

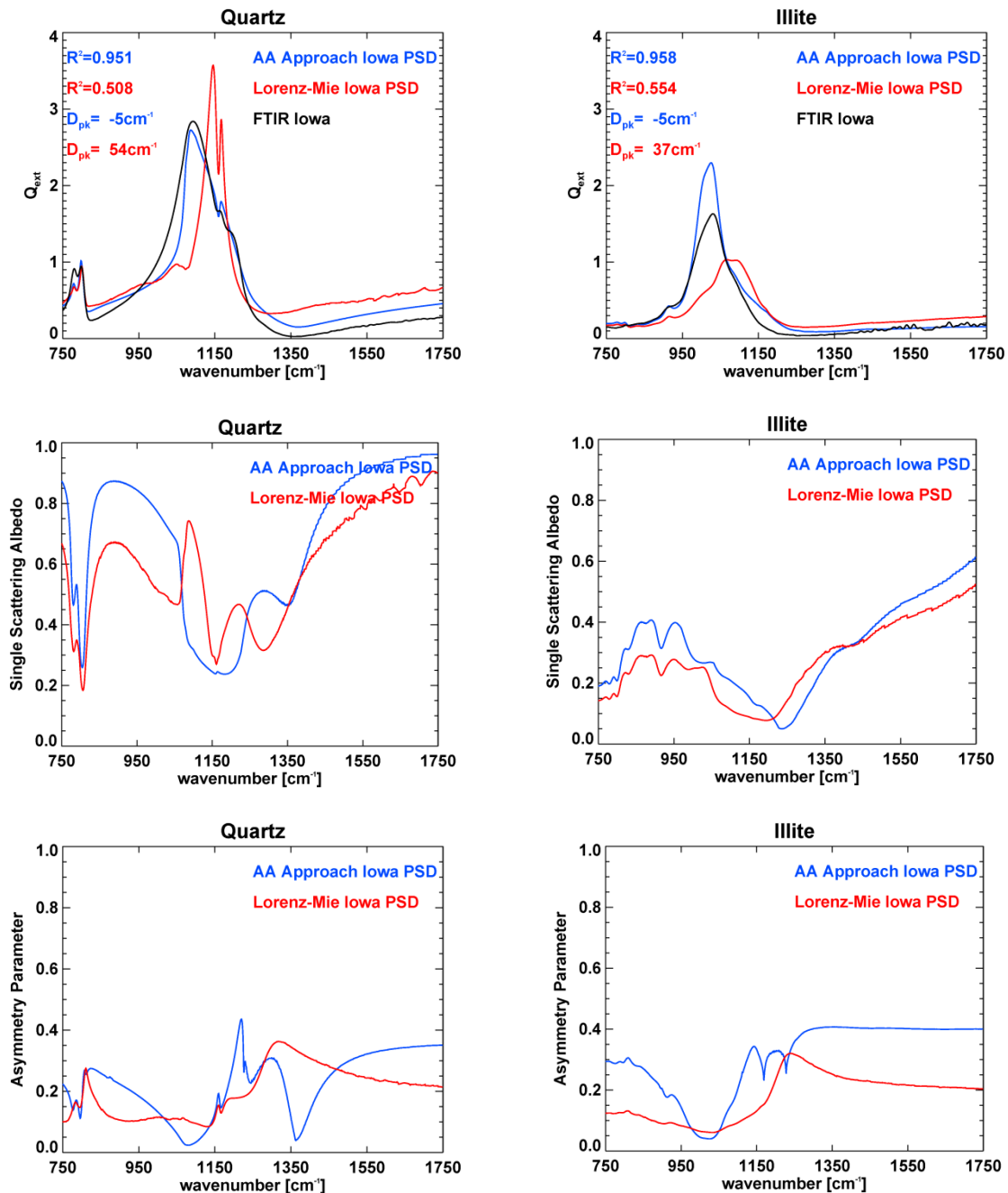


Figure 6: Extinction efficiency (top), single scattering albedo (middle) and asymmetry parameter (bottom) for quartz (left) and illite (right) as simulated with the AAA method (blue) and Lorenz-Mie theory (red) as well as corresponding laboratory measurements of the University of Iowa (black) in



the terrestrial IR spectral region. The spectra and size distributions correspond to the measurements described in [Mogili et al., 2008].

Analogously Figure 7 shows extinction spectra of kaolinite-rich (“Niger”) and illite/quartz-rich (“China”) bulk dust samples in the terrestrial infrared window region as simulated with the AAA method, with Lorenz-Mie theory as well as measurements from an atmospheric simulation chamber (as described in [Klüser et al., 2016]). The two spectra for each mixture reflect the evolution of the spectral extinction during the residence time within the chamber (see [Di Biagio et al., 2014]). These spectra clearly highlight the benefit of the AAA method for hyperspectral TIR remote sensing ([Klüser et al., 2016]).

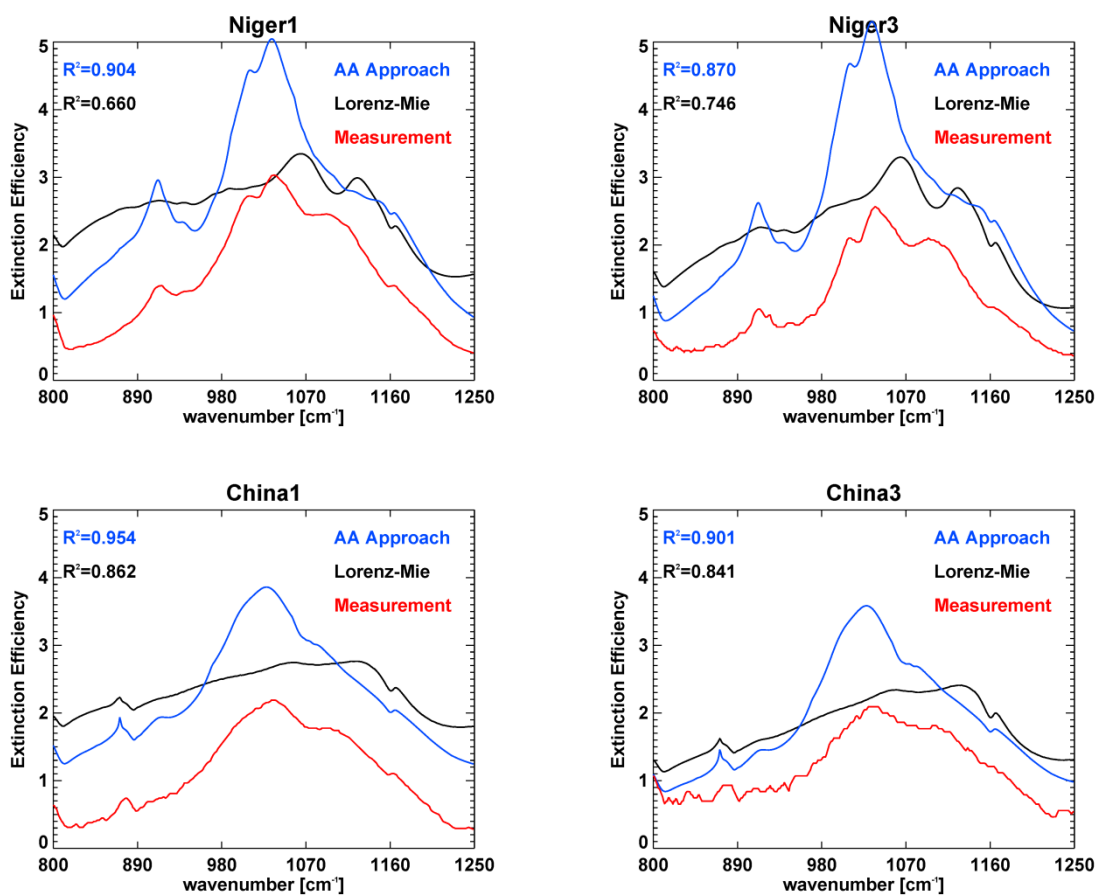


Figure 7: Extinction efficiency spectra of kaolinite rich (top) and illite/ quartz rich (bottom) dust samples as simulated with the AAA method (blue) and Lorenz-Mie theory (black) as well as corresponding laboratory measurements of the University of Paris East (red) in the terrestrial IR window region. The figures correspond to dust extinction directly after injection into the atmospheric simulation chamber (left) and after 50 minutes residence time (right) and consequently to different size distributions as larger particles deposit faster (see [Klüser et al., 2016]).



3.1.5 Theoretical considerations of the IMARS retrieval approach

The mathematical approach of IMARS v7.1 is based on forward simulations of various dust realizations, the resulting brightness temperature differences (see section 1.2) of which are kept in look-up tables (LUTs). The realizations include varying dust particle size distributions and mineralogical compositions as outlined earlier, and also 5 different dust layer altitudes, expressed in the radiance ratio of blackbody emission characterized by the dust layer temperature and the surface temperature as well as varying dust TIR AOD. Although it depends on the surface temperature, the altitude range covered by the approach is typically between 500m and 6km. The AOD range (TIR) covered varies between 0.01 and 3. The forward simulations are performed with the Two-Stream solution (eq.(2)) using AAA optical properties as outlined earlier and described in detail in [Klüser et al., 2016], examples for ocean and desert surface emissivities and for different thermal contrasts between dust layer and surface are presented in Figure 8.

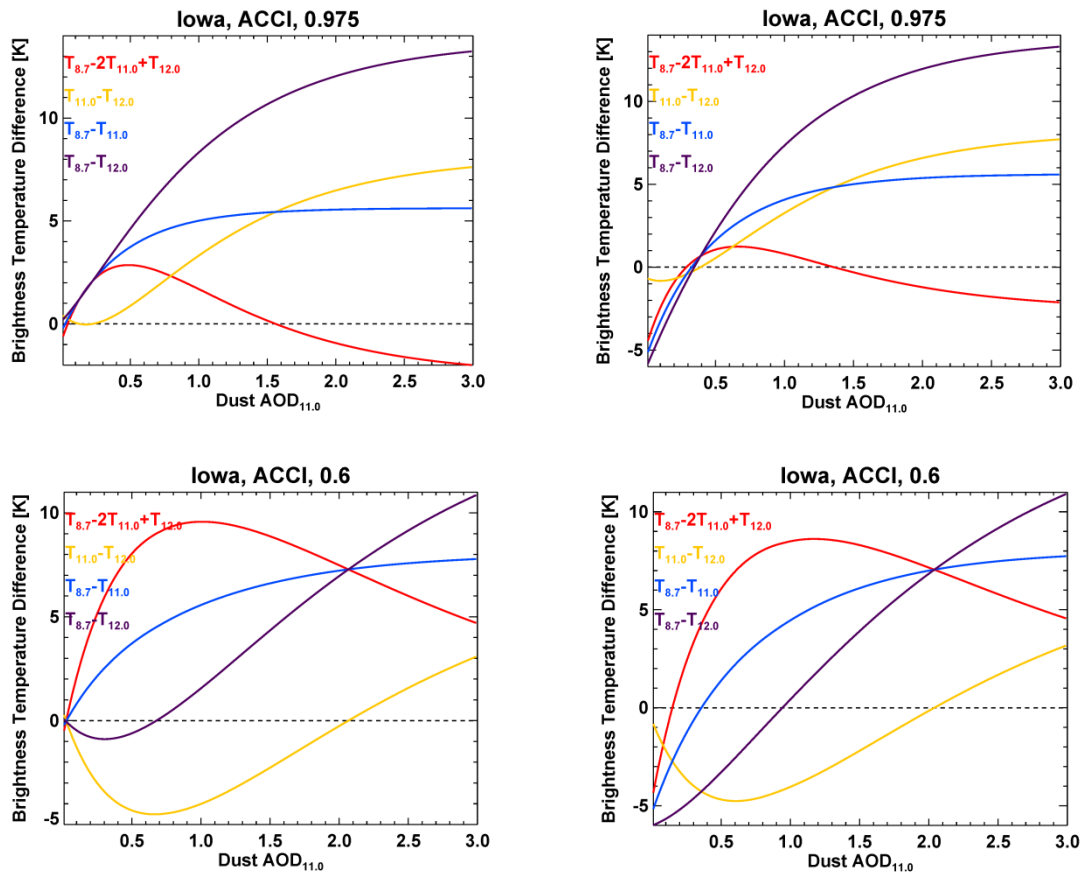


Figure 8: Example of simulated brightness temperature differences for various TIR AODs. These simulations have been performed with the “Iowa Loess” mixture and the lognormal “Aerosol_cci” particle size distribution for ocean (left) and desert (right) surface emissivities and for near-surface dust (approx. 500m, top) and an elevated dust layer (approx. 5km, bottom).

Based on these pre-tabulated look-up tables the IMARS retrieval generates a probability density function (PDF) over the full space of dust realizations. For each fixed dust particle size (index s), dust



composition (index c) and dust layer height (index h) a partial probability for each AOD from each BTM is generated with a Gaussian :

$$P_i(s, c, h, \tau) = \frac{1}{\sigma_i(s, c, h)\sqrt{2\pi i}} \exp \left[-0.5 \left(\frac{\widehat{BTD}_i(s, c, h, \tau) - BTD_i}{\sigma_i(s, c, h)} \right)^2 \right]. \quad (45)$$

Here the subscript i is the index of the brightness temperature difference, BTD_i is the observed brightness temperature difference, \widehat{BTD}_i is the simulated brightness temperature difference and σ_i is the assumed noise level in BTD_i . In IMARS the noise level is set to 10% of the root-mean-square deviation from largest signal (i.e. BTM with the highest AOD) for all four brightness temperature differences.

It is assumed in the IMARS retrieval that the information conveyed by each of the the four brightness temperature differences is independent from one another, although only three channels are used as input; three out of four BTM express the differences between two channels and one contains information of all three bands. Under this assumption, the LUT joint probability for each $\{s, c, h, \tau\}$ is just the product of the four “partial” (i-) probabilities, i.e

$$P(s, c, h, \tau) = \prod_{i=1}^4 P_i(s, c, h, \tau), \quad (46)$$

and it is subsequently normalized with respect to τ , and reassigned to $P(s, c, h, \tau)$. IMARS creates a PDF over the set $\{s, c, h\}$, thus the probability has to be aggregated over τ and an AOD value has to be assigned. This is done by taking weighted averages with respect to the corresponding τ -probability:

$$P(s, c, h) = \sum_j \left(P(s, c, h, \tau_j) \right)^2 \quad (47)$$

$$\tau^*(s, c, h) = \frac{\sum_j (P(s, c, h, \tau_j) \cdot \tau_j)}{\sum_j P(s, c, h, \tau_j)}. \quad (48)$$

$P(s, c, h)$ describes the PDF over size, composition and altitude of the observed dust with TIR AOD τ^* . The final retrieved dust properties are then acquired by summation with respect to the corresponding dimension(s):

$$R_{eff} = \sum_c \sum_s P(s, c) \cdot \widehat{R}_{eff}(s, c), \quad (49)$$

$$D_{mw} = \sum_c \sum_s P(s, c) \cdot \widehat{D}_{mw}(s, c), \quad (50)$$

$$T_{dust}(h) = \sum_h P(h) \cdot \widehat{T}_{dust}(h), \quad (51)$$

$$\gamma = \sum_s \sum_c \sum_h P(h) \cdot \tau^*(s, c, h), \quad (52)$$

$$AOD_{TIR} = \sum_s \sum_c \sum_h P(h) \cdot \tau^*(s, c, h), \quad (53)$$

$$AOD_{0.55\mu m} = \gamma \cdot AOD_{TIR}, \quad (54)$$

where γ denotes the composition- and size-dependent ratio between TIR and visible (0.55 μ m) AOD. The dust mass column is estimated by calculating an infrared mass extinction efficiency ($= \frac{4\rho_{dust}R_{eff}}{3Q_e}$, where ρ_{dust} is the density of dust aerosol) based on composition and particle size analogous to Eq. (44)-(46) and then multiplying AOD_{TIR} with the infrared mass extinction efficiency (see [Petty, 2006]). The density of quartz (2.65 g/m³) has been used as ρ_{dust} for mass column calculation, as the densities of other silicates do not vary much from this value.



The overall dust probability P_{dust} is defined analogously (e.g. see Eq. (47)) as the weighted average of all non-zero $\{P(s,c,h)\}_{s,c,h}$. An auxiliary expectation value $\hat{t}^*(s,c,h)$ is calculated exactly like the Eq. (49)-(51) and, using it, we define the (early stage) retrieval uncertainty (ε_{dust}) as the weighted standard deviation of $\hat{t}^*(s,c,h)$. Furthermore, the uncertainties for AOD_{TIR} , $AOD_{11\mu m}$ and $AOD_{0.55\mu m}$ are calculated by using corresponding auxiliary expectation values as well as using common error propagation method to combine these intermediate independent (assumed) uncertainties accordingly. For instance, in order to find the uncertainty for $AOD_{0.55\mu m}$, the intermediate expectation values and uncertainties for γ and AOD_{TIR} should be taken into account.

Using the concept of channel capacity (CC), the information rate over communication channels, which are considered here to be identical to our (three) pseudo-channels, can be calculated by

$$CP = 3 \log_2 \left(\frac{\hat{t}^* + \varepsilon_{dust}}{\varepsilon_{dust}} \right). \tag{55}$$

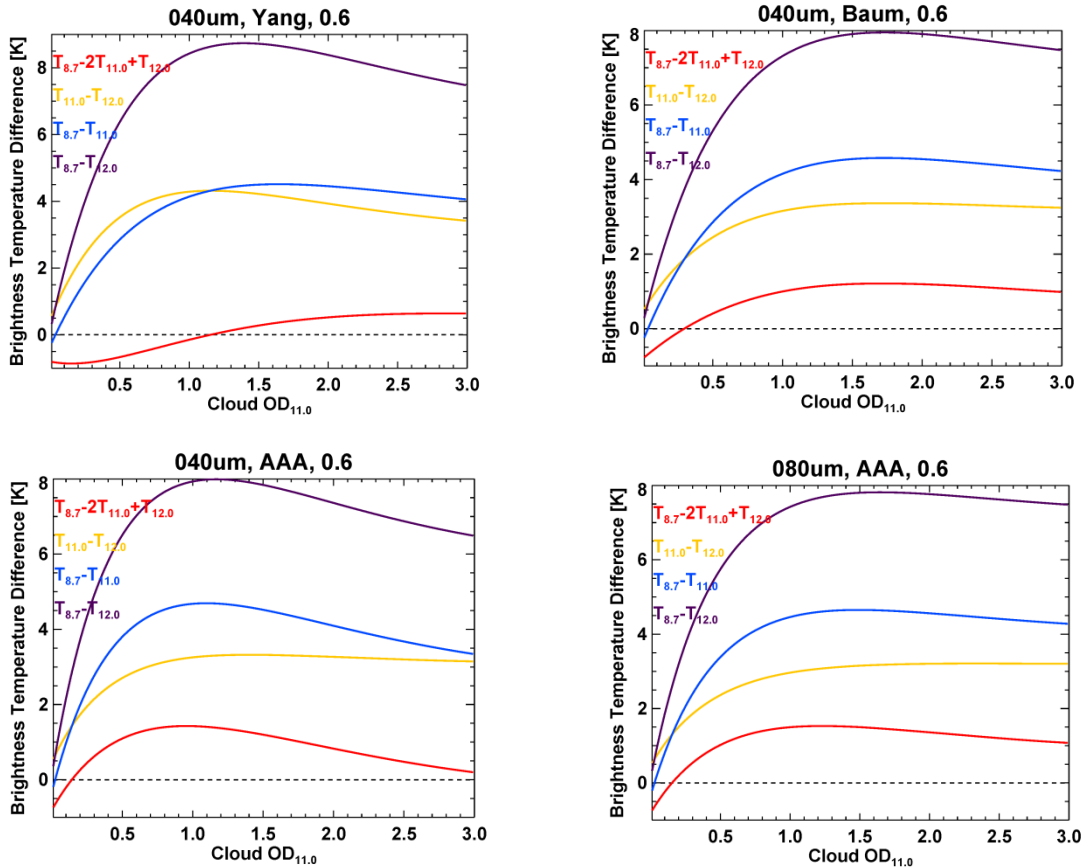


Figure 9: Example of simulated brightness temperature differences for various TIR ice cloud optical depths. These simulations have been performed for ocean surface emissivities at a moderate cloud height of (approx. 5km, bottom). Brightness temperature differences have been simulated for ice cloud with an effective diameter of 40 μm with the parameterizations of *Yang et al. 2005* (top left), *Baum et al. 2013* (top right), and the AAA disk model (bottom left). For the latter also the impact of crystal size of the BTD is exemplarily presented for simulations with an effective radius of 80 μm .



An ice cloud retrieval is performed in exactly the same way. The ice cloud optical properties are calculated for four effective radius values of 10 μ m, 40 μ m, 80 μ m, 100 μ m and with three different parameterizations assuming different shape models. The parameterizations are the *Yang et al.* model ([Yang et al., 2005]), the *Baum et al.* model ([Baum et al., 2014]) and the AAA disk model.

For all variables like probability, retrieval uncertainty, optical depth, emission temperature etc. two values are available in IMARS: one for dust and one for (ice) clouds. However, currently, the ice-cloud retrieval includes only the (early stage) retrieval uncertainty. The probabilities of dust and cloud are fed into another derived variable, namely, the retrieval entropy H . This quantity, introduced by [Shannon, 1949] and further analyzed in [Shannon and Weaver, 1949], is often also referred to as the (Shannon) information content. In the case of IMARS the retrieval entropy is defined similarly to the information spectrum (Eq. (9)) as

$$H = -(P_{dust} \cdot \log_2(P_{dust}) + P_{cloud} \cdot \log_2(P_{cloud})) \quad (56)$$

It describes the distinguishability between dust and cloud and thus the reliability of the a posteriori discrimination. The lower the entropy, the more reliable the discrimination (toward either end) is. High entropy indicates a non-reliable discrimination and the retrieval results should be used with great caution. Reasons for high entropy can be low optical depths (and thus an atmosphere containing neither significant amounts of dust nor ice cloud) or a spectral signal which is out of reach for IMARS, e.g. signals governed by surface emissivity or dominant gas absorption. Furthermore, entropy plays a role in IMARS quality flagging as part of a posterior quality assessment.

At the final stage of IMARS algorithm, we seek to correct P_{dust} taking into account P_{cloud} and vice versa. Only in this sense, the possibility of “neither dust nor cloud” is considered negligible and the corrections take the form of a geometric mean as follows:

$$\tilde{P}_{dust} = \sqrt{P_{dust}(1 - P_{cloud})}, \quad (57)$$

$$\tilde{P}_{cloud} = \sqrt{P_{cloud}(1 - P_{dust})}. \quad (58)$$

The latter are obviously first-order corrections since having “dust” or “cloud” are generally not mutually exclusive events. Note that after this point we will refer to \tilde{P}_{dust} and \tilde{P}_{cloud} as the corrected dust- and cloud probabilities respectively. Finally, within the posterior quality assessment process, we scale AOD, COD and other retrieval products based on pixel location (in/out of dustbelt) using empirical factors which depend on Eq. (57) and (58), see section 3.2.5.

3.2 Implementation

3.2.1 IMARS processing environment

The currently used and herein described retrieval implementation refers to version 7.1 of the IMARS algorithm. Version 5 and beyond distinguishes itself from all lower versions in that it is no longer based on principal component decomposition of simulated (or observed) IASI spectra but that forward simulations with different dust AOD and dust layer altitude (in terms of thermal contrast between ground and dust) are evaluated in a probabilistic way in order to acquire dust information from the IASI observations. Moreover, due to high redundancy in the IASI spectra, it uses four pseudo-channels centered at central wavelengths of typical narrowband imaging instruments. Version 7.0 and beyond operates entirely in python programming language in contrast to all previous versions operating in IDL, Fortran and Bash scripts pertaining to different parts of the processing chain. While



the main architecture remains mostly as it is, the code changed drastically and was optimized to support parallelization schemes in all levels. Moreover, the preprocessing part is now fully autonomous in the sense that it operates with new internal reading-routines (python) and not the ones provided by EUMETSAT (IDL).

The IMARS v7.1 processing environment consists of a core program (referred to as “IMARS”) performing the aerosol/cloud retrieval, a couple of preprocessors for extracting the required information from IASI L1C spectra in native file format and a postprocessor for casting the generic IMARS output to the exact file format specified for aerosol_cci and for producing output at higher data levels - Level-3 for example), all of which are implemented in python for the first time. Note that the generation of look-up tables and optical properties has been implemented in IDL for previous versions and is left and used as it is. Note, further, that the entire program structure of IMARS core and the pre/postprocessors, previously (v<=6.0) written in FORTRAN and IDL respectively, was kept almost identical.

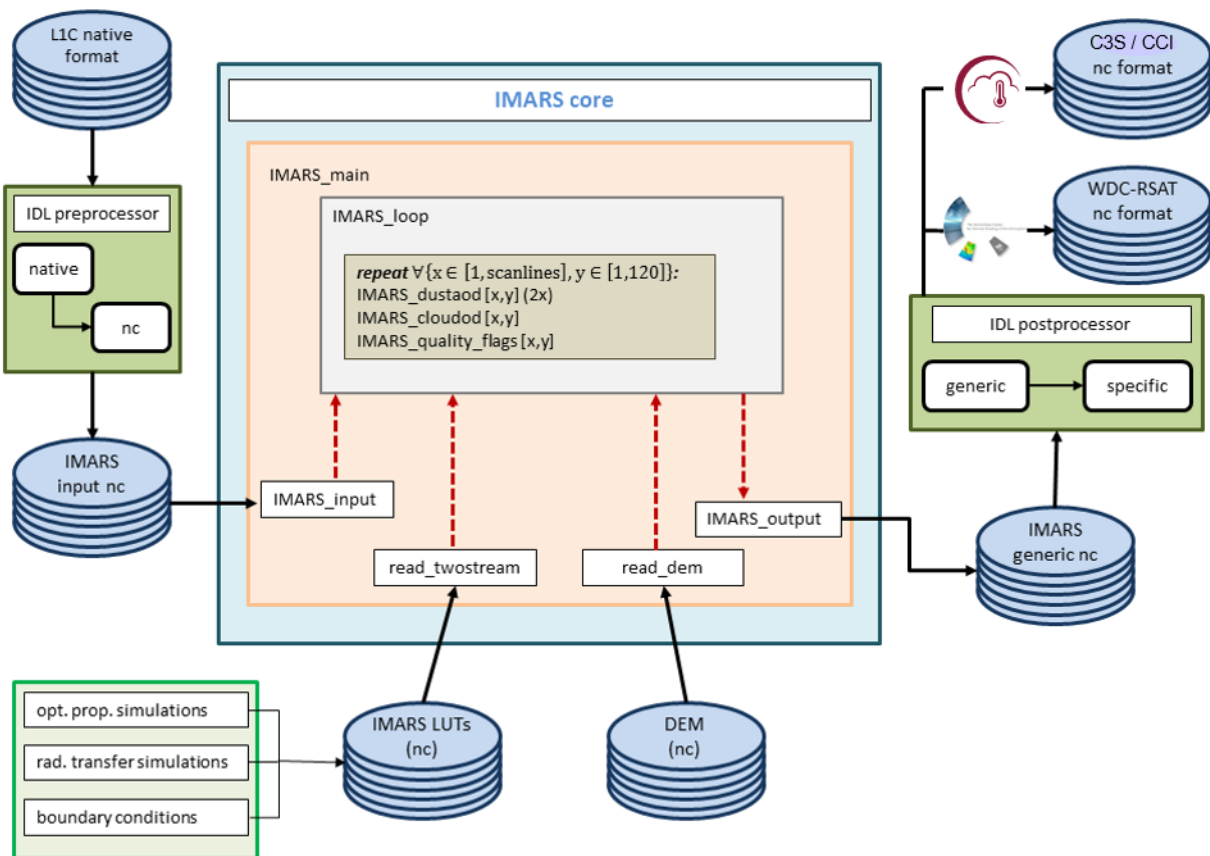


Figure 10: Overview of the IMARS processing environment.



3.2.2 Preparatory steps

By performing offline Two-Stream simulations, lookup tables are created as described before. The simulations include properties for dust or ice clouds combined with ocean (assumed to be very similar to vegetation, as both have low spectral contrast) and dust combined with desert surface emissivities (see section 3.1.3).

IASI Level 1 full resolution spectra provided by EUMETSAT are used to generate the input for IMARS (see section 3.2.1).

IASI radiance observations are collected into 28 bins represented by the maximum brightness temperature as described before. The bin collection is executed within a separate preprocessor, as it is not necessary to repeat this time consuming step for each algorithm update.

The retrieval is done separately for each observed spectrum and thus can be applied in any granularity of the input data without constraints on spatial coverage. The first step is then to aggregate the bins into the four scaled brightness temperature differences needed for the retrieval.

3.2.3 Surface emissivity

Example surface emissivities for ocean and desert surfaces have been compiled from the MODIS UCSB Emissivity Library of the Institute for Computational Earth System Science (ICESS) at the University of California, Santa Barbara (UCSB). They can be accessed online⁴ and include spectra of water, ice and snow surfaces, soils and minerals as well as vegetation. As no prior land use atlas is applied, the retrieval is run twice over land. Once with emissivity values of vegetated surfaces (low spectral contrast, ocean emissivity is used as proxy) and once with values representing deserts (high spectral contrast). The results are weighted according to their relative dust probabilities. As ice clouds have inverse spectral behaviour the two-step approach is omitted for clouds, i.e. no specific cloud retrieval with desert emissivities is performed.

3.2.4 Implementation of the core dust retrieval

IMARS uses a priori cloud masks (thus the module “imars_cloudmask” in Figure 11) as well as an a posteriori cloud screening. IASI IMARS cloud detection is entirely based on the a posteriori quality and probability information provided by the retrieval itself. In terms of the retrieval methodology that means, that for every IASI FOV two retrieval chains (as described in section 3.2.5) are run independently, one for dust and one for ice clouds. Only after full information about dust and clouds, particularly about probabilities and uncertainties, is available, quality assessment of both retrieval branches can begin. The final step for this assessment is a decision whether a FOV is more likely to contain dust or cloud or none of the latter (low quality implied). The generation of quality flags and cloud filtering is described below in sections 3.2.5 and 3.2.6, respectively. The IMARS core algorithmic chain is depicted schematically in Figure 11.

⁴ <http://www.icess.ucsb.edu/modis/EMIS/html/em.html>, last accessed 30/11/2023

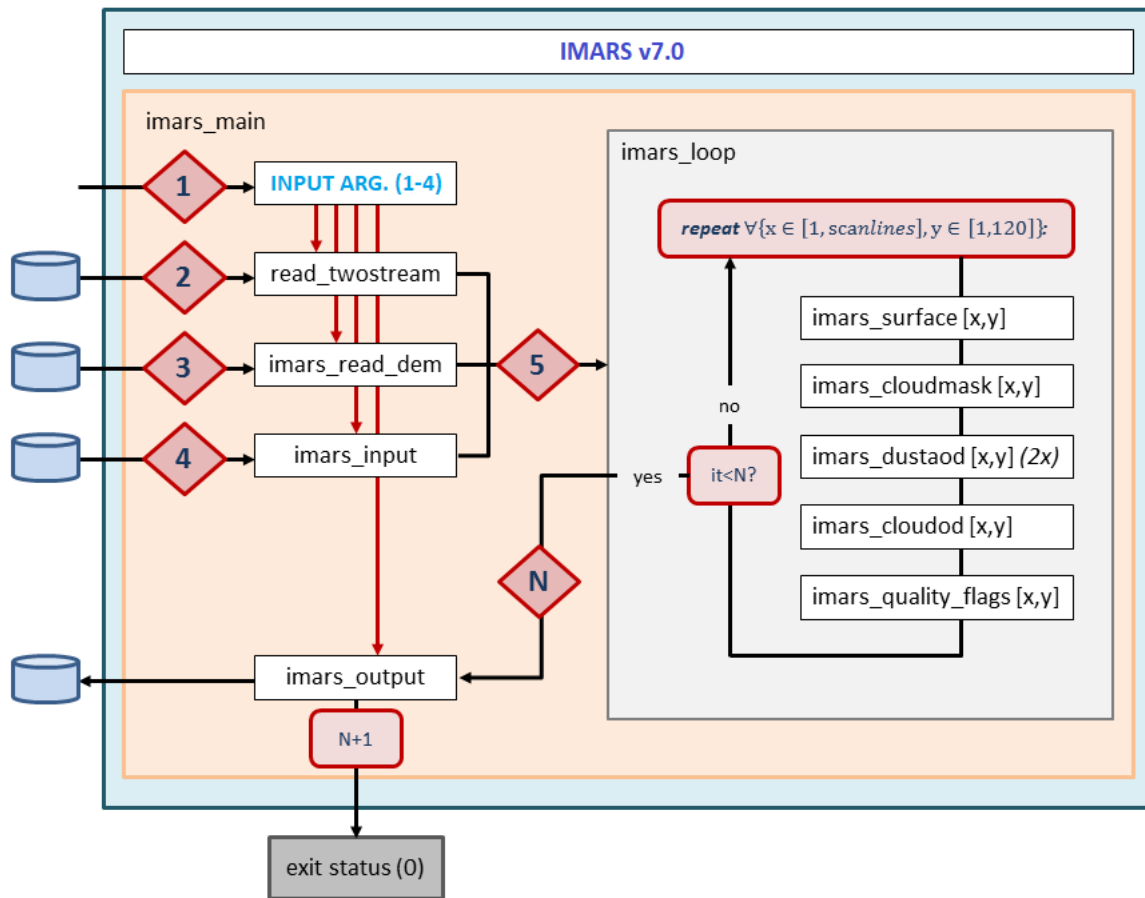


Figure 11: Program flow chart of the IMARS retrieval (identical for v7.0 and v7.1). The retrieval loop is repeated for all FOVs per scanline and for all scanlines of the granule/orbit. This flow chart is a close-up of the blue box (“IMARS Core”) in Figure 10.

Figure 12 depicts the algorithmic design of the retrieval flow per FOV. Starting from the observations, the four scaled brightness temperature differences are used as input independently for the dust and the ice cloud retrieval chain. Only after both return results (which always pertain to non-zero optical depth by design), their quality is assessed by generating independent quality flags for dust and ice clouds and by calculating the retrieval entropy (Eq. (56)). After all information (physical, probabilistic and quality) is available, the assessment if the FOV contains most likely dust or ice cloud or none of the latter is performed.

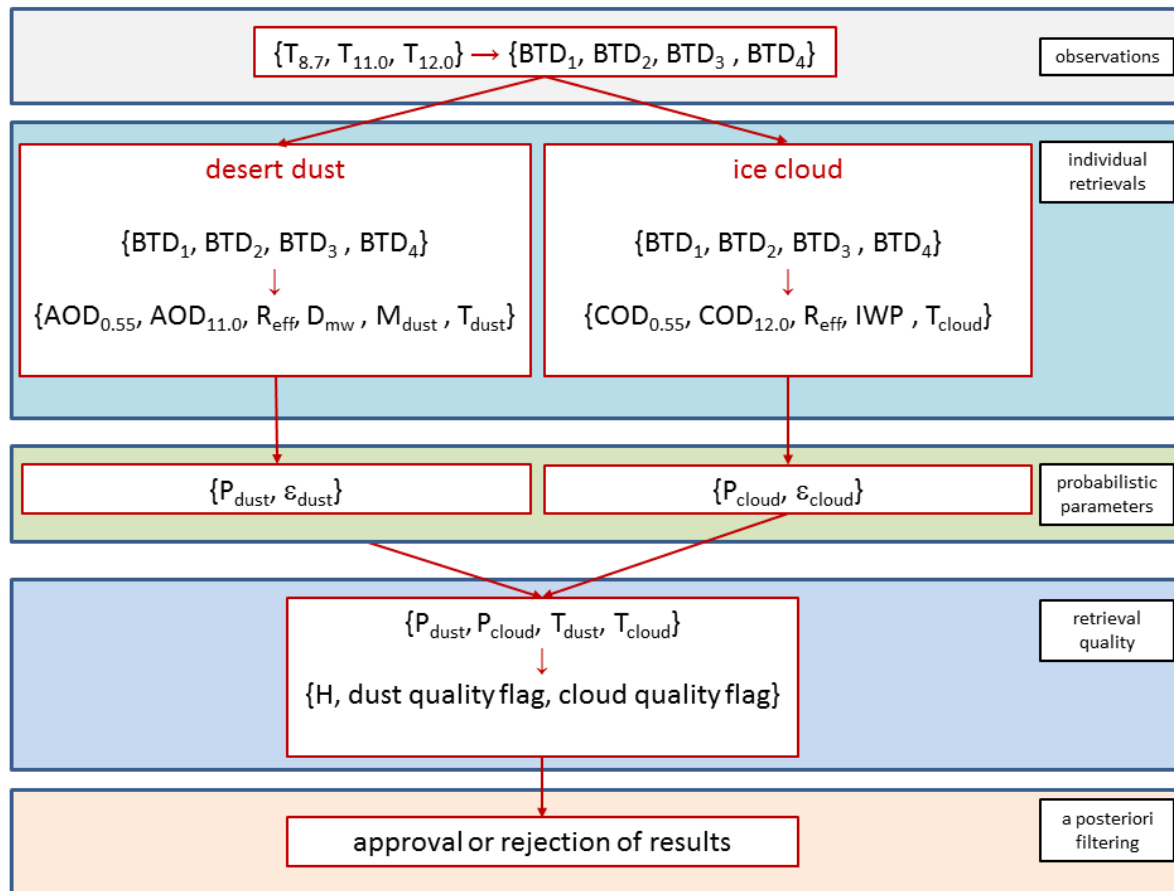


Figure 12: Modular design of the IMARS version 7.1 algorithm chain independently performed for each FOV. This module plot is a schematic close-up of the white box (“imars_loop”) in Figure 11.

3.2.5 Quality Flags

Quality flags are derived for mineral dust and ice cloud observations separately based on the same physical principles. In general, an observation is assumed to be reliable, if the (early stage) retrieval uncertainty ϵ is small, the probability estimate is high and the emission temperature is within an expected range (cold for ice clouds, rather warm for desert dust), and less reliable if the information entropy is high. Moreover the comparison of quality indicators for dust is used for assessing the possibility of contamination by clouds and vice versa. The conditions for quality flag increase/decrease are presented in Table 7. The value of the quality flag (QF) is raised by 1 if any of the conditions below (except of the entropy-related) is fulfilled and only reduced by 1 if entropy is high and QF is already at least 1. Consequently a QF value of 0 indicates absolutely unreliable conditions (generally no values are retrieved at all) and QF=10 indicates perfect conditions with the highest level of reliability (see also Table 7). Quality flags for desert dust (DQF) and ice clouds (CQF) are formulated analogously, as also the building blocks of the retrieval follow the exact same algorithm. Consequently the resulting quality flags for dust and cloud are fully comparable and rely on the same intrinsic quality measures.



Table 7: Quality flag conditions in IMARS

Conditions for increasing mineral dust QF	Conditions for increasing ice cloud QF
$P_{dust} > 0.25$ and $P_{cloud} < 0.75$	$P_{cloud} > 0.25$ and $P_{dust} < 0.75$
$P_{dust} > 0.5$ and $P_{cloud} < 0.5$	$P_{cloud} > 0.5$ and $P_{dust} < 0.5$
$P_{dust} > 0.75$ and $P_{cloud} < 0.25$	$P_{cloud} > 0.75$ and $P_{dust} < 0.25$
$\epsilon_{dust} < 0.5$ and $P_{dust} > 0.25$ and $T_{dust} > 240K$	$\epsilon_{cloud} < 0.5$ and $P_{cloud} > 0.25$ and $T_{cloud} < 270K$
$\epsilon_{dust} < 0.3$ and $P_{dust} > 0.5$ and $T_{dust} > 240K$	$\epsilon_{cloud} < 0.3$ and $P_{cloud} > 0.5$ and $T_{cloud} < 270K$
$\epsilon_{dust} < 0.5$ and $CC(dust) > CC(cloud)$ and $T_{dust} > 240K$	$\epsilon_{cloud} < 0.5$ and $CC(cloud) > CC(dust)$ and $T_{cloud} < 270K$
$\epsilon_{dust} < 0.3$ and $CC(dust) > CC(cloud)$ and $T_{dust} > 240K$	$\epsilon_{cloud} < 0.3$ and $CC(cloud) > CC(dust)$ and $T_{cloud} < 270K$
$P_{dust} > P_{cloud}$ and $CC(dust) > CC(cloud)$ and $CC(dust) > 3$	$P_{cloud} > P_{dust}$ and $CC(cloud) > CC(dust)$ and $CC(cloud) > 3$
$\epsilon_{dust} < 0.5$ and $P_{dust} > P_{cloud}$ and $CC(dust) > CC(cloud)$ and $T_{dust} > 280K$	$\epsilon_{cloud} < 0.5$ and $P_{cloud} > P_{dust}$ and $CC(cloud) > CC(dust)$ and $T_{cloud} < 270K$
$\epsilon_{dust} < 0.3$ and $P_{dust} > P_{cloud}$ and $CC(dust) > CC(cloud)$ and $T_{dust} > 260K$	$\epsilon_{cloud} < 0.3$ and $P_{cloud} > P_{dust}$ and $CC(cloud) > CC(dust)$ and $T_{cloud} < 250K$
$QF > 0$ and $H > 0.75$	
$QF > 0$ and $H > 0.95$	

As in IMARS v7.0, probabilities for the dust or cloud classification were also added to an alternative postprocessing weighting. The direct weighting of v7.0, by multiplying the respective probability with the pixel value, was exchanged for v7.1 for an uneven scaling formula based on the pixel’s cloud or dust probability. IMARS v7.0 results had shown a sharp decline in dust/cloud classification accuracy towards lower percentage values of the respective classification probability. Probabilities near 100% or 0% were deemed accurate in a vast majority of cases. In the mid-range of probability values around 30-70% a misclassification of clouds as dust observations was often present. Simultaneously, the complementary cloud probability was also low, which is likely why the retrieval chose afflicted pixels as dust in the first place.

An improvement of the handling of these middling probability cases was achieved after improving the probability scaling from a linear multiplication to an uneven scaling function with the formula

$$y = 1 - \frac{1}{e^{\frac{x-0.6}{0.05}} + 1} \tag{59}$$

Where x is the respective probability, P_{dust} or P_{cloud} , and y the scaling factor that is then multiplied with the dust or cloud data value. The formula describes an S-shaped curve that is tailored to keep values with probabilities 80% < nearly unchanged, but causes a sharp decline with the half-way mark at 60%. Values at <40% probability are suppressed and the algorithm implementation allows for an interval to be defined where values within the given probability interval are set to zero or NaN, depending on the function call. With v7.1 this interval has been set to $[0.0, 0.35]$ by default and in accord with other parts of the retrieval, values are returned as zero.

In effect, the algorithm handles the scaling, using the formula from equation 59, like this:

$$AOD \rightarrow AOD * y(P_{dust}) \text{ for } P_{dust} = \{0.35 \leq x\}$$



$$\begin{aligned} \text{AOD} &\rightarrow 0.0 \text{ for } P_{\text{dust}} = \{0.0 \leq x < 0.35\} \\ M_{\text{dust}} &\rightarrow M_{\text{dust}} * \gamma(P_{\text{dust}}) \text{ for } P_{\text{dust}} = \{0.35 \leq x\} \\ M_{\text{dust}} &\rightarrow 0.0 \text{ for } P_{\text{dust}} = \{0.0 \leq x < 0.35\} \\ \text{COD} &\rightarrow \text{COD} * \gamma(P_{\text{cloud}}) \text{ for } P_{\text{cloud}} = \{0.35 \leq x\} \\ \text{COD} &\rightarrow 0.0 \text{ for } P_{\text{cloud}} = \{0.0 \leq x < 0.35\} \\ \text{CWP} &\rightarrow \text{CWP} * \gamma(P_{\text{cloud}}) \text{ for } P_{\text{cloud}} = \{0.35 \leq x\} \\ \text{CWP} &\rightarrow 0.0 \text{ for } P_{\text{cloud}} = \{0.0 \leq x < 0.35\} \end{aligned}$$

These empirical assignments have no strong theoretical basis but instead follow observed retrieval behaviour and validation results.

3.2.6 A posteriori cloud discrimination and approval of results

Cloud screening is performed *a posteriori* based on the retrieval results. Basically it is done by comparing channel capacity and quality flags for dust and clouds, partially bound by retrieved optical depth (AOD or COD) and probabilities. The dust/cloud discrimination tests listed in Table 8 form a basis of “dust-“ and “cloud conditions” (No. 1, 2), makes a final attempt to label some un/misclassified (neither dust nor cloud) pixels to either dust or cloud ones (No. 1, 2, 3), depending on AOD/COD values and probabilities), and leaves the rest as they are.

Table 8: Quality flag decisions in IMARS

Test No.	Test conditions	Decision
1	(AOD>0 and DQF>1 and CC (dust)>CC (cloud))	“dust”
2	(COD>0 and CQF>1 and CC (cloud)>=CC (dust))	“cloud”
3	(None of 1, 2 and AOD>0.05 and DQF>1 and $P_{\text{dust}} > P_{\text{cloud}}$)	“dust”
4	(None of 1, 2 and COD>0.2 and CQF>1 and $P_{\text{cloud}} > P_{\text{dust}}$)	“cloud”
5	(None of 1,2 and AOD>0 and DQF>2)	“dust”

3.3 Retrieval examples

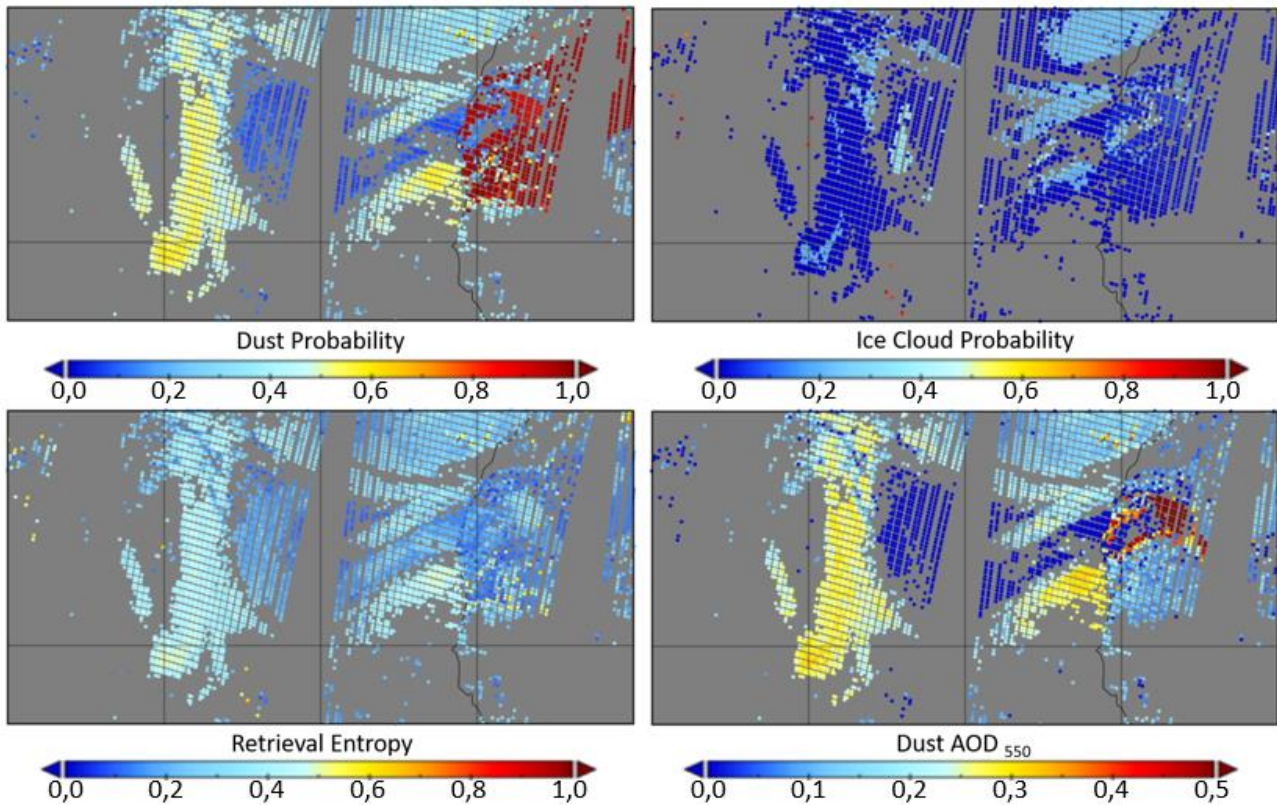


Figure 13: IMARS v7.1 results for P_{dust} (top left) and P_{cloud} (top right) and H (bottom left) as well as dust $AOD_{0.55\mu m}$ (bottom right) for the large dust outbreak off the coast of West Africa on 17 September 2010 observed with IASI on board Metop-A.

A strong large-scale dust outbreak from the West Sahara to the Atlantic Ocean is shown in terms of IMARS retrieval results in Figure 13. Dust and ice cloud probabilities are shown exemplarily, indicating the confidence in the positions of the dust plume and deep convective clouds. Moreover the retrieval entropy H (Shannon information content) and dust $AOD_{0.55\mu m}$ are presented. Dust properties (P_{dust} , $AOD_{0.55\mu m}$) are depicted only for FOVs identified containing dust as described in Section 3.2.5 and P_{cloud} is shown for cloudy observations only. Grey IASI FOVs scale with T_{base} so that low baseline temperatures appear dark grey while higher ones light grey. Grey scale is applied in the case of no successful retrieval available. It is clearly evident that also H conveys very useful information for the interpretation of the retrieval results and it is thus a source of additional valuable quality information. In the case of the deep convective cloud cores (especially the two hurricanes in the western part of the plot) P_{dust} is so low that H becomes mathematically unstable and it is then depicted to be missing information (greyscale areas in H plot). Regarding the dust plume it can be seen that the value of H is low when it is clear that the observation is dust and not cloud (e.g. over the high dust AOD areas and over the Sahara desert). On the other hand, regions characterized by high H represent observations where not much trust can be granted for the discrimination between dust and clouds. This is not necessarily connected to low optical depths returned by the retrieval (e.g. over continental South America). A more detailed discussion on guidelines for using the quality information in IMARS can be found in chapter 4.3.



4 Algorithm output

IMARS output follows the guidelines given in PUGS [RD1]. The latest version is accessible online⁵.

4.1 Generic IMARS output

Table 9: Output field variable names contained in the generic IMARS output.

Output fields	Dim.	Type	Scale	Content
"latitude"	SLx120	Flt32	1.0	Latitude of FOV center
"longitude"	SLx120	Flt32	1.0	Longitude of FOV center
"VZA"	SLx120	Flt32	1.0	Viewing zenith angle for FOV center
"UTC"	SLx120	Flt32	1.0	UTC time of observation (milliseconds)
"Elevation"	SLx120	Flt32	1.0	Average surface elevation of FOV
"Landmask"	SLx120	Int16	1	Landmask for IASI FOV
"Tbase"	SLx120	Int16	10	FOV Baseline temperature
"Entropy"	SLx120	Int16	10 ²	Retrieval entropy
"DQF"	SLx120	Int16	1	Dust quality flag
"DCC"	SLx120	Int16	10 ²	Dust channel capacity
"DAOD550"	SLx120	Int16	10 ³	Dust AOD at 0.55µm
"DAOD10"	SLx120	Int16	10 ³	Dust AOD at 10µm
"DAOD11"	SLx120	Int16	10 ³	Dust AOD at 11µm
"Dmass"	SLx120	Int16	10 ²	Dust mass column
"DReff"	SLx120	Int16	10 ²	Dust effective radius
"DMWMD"	SLx120	Int16	10 ³	Dust mass-weighted mean diameter
"DLT"	SLx120	Int16	10	Dust layer effective temperature
"DProbability"	SLx120	Int16	10 ³	Dust probability
"DUncertainty"	SLx120	Int16	10 ²	Dust retrieval uncertainty (early stage)
"DAOD550_Uncertainty"	SLx120	Int16	10 ²	Uncertainty for Dust AOD at 0.55 µm
"DAOD10_Uncertainty"	SLx120	Int16	10 ²	Uncertainty for Dust AOD at 10 µm
"DAOD11_Uncertainty"	SLx120	Int16	10 ²	Uncertainty for Dust AOD at 11 µm
"DQuartzFraction"	SLx120	Int16	10 ³	Quartz abundance in dust
"DilliteFraction"	SLx120	Int16	10 ³	Illite abundance in dust
"DKaoliniteFraction"	SLx120	Int16	10 ³	Kaolinite abundance in dust
"DMontmorilloniteFraction"	SLx120	Int16	10 ³	Montmorillonite abundance in dust
"DFeldsparFraction"	SLx120	Int16	10 ³	Feldspar abundance in dust
"DCalciteFraction"	SLx120	Int16	10 ³	Calcite abundance in dust
"CQF"	SLx120	Int16	1	Cloud quality flag
"CCC"	SLx120	Int16	10 ²	Cloud channel capacity
"COD550"	SLx120	Int16	10 ³	COD at 0.55µm
"COD12"	SLx120	Int16	10 ³	COD at 12µm

⁵ http://wdc.dlr.de/C3S_312b_Lot2/Documentation/AER/C3S2_312a_Lot2_PUGS_AER_latest.pdf



“CWP”	SLx120	Int16	10	(Ice) Cloud water path
“CReff”	SLx120	Int16	10 ²	(Ice) Cloud effective radius
“CTT”	SLx120	Int16	10	Cloud top temperature
“CProbability”	SLx120	Int16	10 ³	Cloud probability
“CUncertainty”	SLx120	Int16	10 ²	Cloud retrieval uncertainty (early stage)

The content of the generic IMARS output is shown in Table 9. The table contains the dataset name in the output files, the dimensions (“Dim.”) of the output as well as the data type (“Type”) and, if applied, a scaling factor (“Scale”). The last column describes the content of the dataset. In the IASI implementation of IMARS the dimensions are all fixed except the number of scanlines (SL) which depends on the granularity of the IASI input format. Each IASI scanline contains 120 Fields-of-View, 30 views from 4 (2x2) detectors (see chapter 1 for more details on instrument characteristics). Scaling factors (SF) are used for casting 32bit floating point variables to 16bit integer in order to save storage memory. Consequently the original value of the variable is obtained through dividing the stored output value by the SF. No offset is used in the data type casting in IMARS. Table 9 is complete with regard to what is generally available in (or may be provided from upon request) IMARS v7.1.

4.2 IMARS CCI / C3S specific output

In order to comply with the CCI data formats and naming convention (which has been adopted by C3S) the IMARS output contains a subset of the resulting variables of the IMARS algorithm while the generic output is stored in generic IMARS data format (netCDF-4 as well) and can be provided upon request. The list of variables together with corresponding dataset names contained in the CCI / C3S IMARS output files is presented in Table 10. The dataset names follow the CCI naming convention, the output data format complies with the CCI data standards and conventions as documented in the Product User Guide and Specification document (PUGS [RD1]). IMARS provides the main dust variables as specified in the PUGS for all IASI algorithms: Dust AOD at 550nm, 10µm and 11 µm, with DAOD uncertainty at 550nm, dust effective radius and dust layer emission temperature as measure of dust height. In addition, IMARS is capable of providing further dust information. Accordingly, additional variables are contained in the files as seen in Table 10 (dust composition, dust probability, etc.) which go beyond the specified C3S main output. These are basically probabilistic variables (dust probability, retrieval entropy), dust size distribution variables (dust mass-weighted mean diameter MWMD), dust emission temperature, dust composition (quartz, illite, kaolinite, montmorillonite, feldspar and calcite fractions) and columnar dust mass. The specification of these dust variables follows (roughly) the naming conventions inherited from the dust variables specified in the PUGS. Geolocation, acquisition time, flags (land, cloud, quality) and global attributes strictly follow the specifications in the PUGS. Furthermore, as of IMARS v7.0, IMARS Level 2 output files include all products of the Generic IMARS output (Table 9), while Level 3 output files still include only an augmented (relative to previous versions) subset of it, see Table 10.



Table 10: Dataset names and contained variables of the aerosol_cci IMARS output files.

Format	
	netCDF4
	the products are compliant with CF metadata convention 1.4 http://cfconventions.org/Data/cf-conventions/cf-conventions-1.4/build/cf-conventions.html
Filename	
	<i>Lv2: daily</i> <year><month><day>-ESACCI-L2_AEROSOL-AER_PRODUCTS-IASI_METOPA-DLR-IMARS_<version>-<OrbitalNode>-<StartSensingTime>_<StopSensingTime>-<fv>.nc
	<i>Lv3, daily (total, optional AM/PM):</i> <year><month><day>-ESACCI-L3C_AEROSOL-AER_PRODUCTS-IASI_METOPA-DLR-IMARS_<version>-<OrbitalNode>-<StartSensingTime>_<StopSensingTime>-<fv>.nc
	<i>Lv3, monthly (total, optional AM/PM):</i> <year><month>-ESACCI-L3C_AEROSOL-AER_PRODUCTS-IASI_METOPA-DLR-IMARS_<version>-<OrbitalNode>-<StartSensingTime>_<StopSensingTime>-<fv>.nc
Global attributes (with examples)	
1	<code>source</code> = "IASI GDS Level 1C" (Level 2) or "IASI IMARS L2" (Level 3)
2	<code>data_type</code> = "swath" (Only for Level 2)
3	<code>cmd_data_type</code> = "grid" (Only for Level 3)
4	<code>summary</code> = "Mineral dust retrieval with the IMARS algorithm" (Level 2) or "Daily/Monthly L3 products of mineral dust retrieval with the IMARS algorithm" (Level 3)
5	<code>product_id</code> = "20080302-ESACCI-L2_AEROSOL-AER_PRODUCTS-IASI_METOPA-DLR-IMARS_v7.1-DN-20080302000000Z_20080302235959Z-fv1.nc" (file name)
6	<code>title</code> = "Infrared Mineral Aerosol Retrieval Scheme (IMARS)"
7	<code>institution</code> = "DLR-DFD"
8	<code>history</code> = "Mi 25. Nov 10:06:55 CET 2020 - Product generated from IMARS v7.1"
9	<code>references</code> = "Aerosol C3S_D312b_Lot2: IMARS-ATBD version 3"
10	<code>tracking_id</code> = "13265243-96e2-473a-94a0-78a6762b7b37" (universally unique identifier)
11	<code>conventions</code> = "CF-1.6"
12	<code>cell</code> = 593040 (example for number of pixels for Level 2), or 360 (1-degree gridded data for Level 3)
13	<code>product_version</code> = "v7.1"
14	<code>keywords</code> = "IASI, Mineral Dust, IMARS"
15	<code>naming_authority</code> = "aerosol.dlr.de"
16	<code>date_created</code> = "Mi 25. Nov 10:06:55 CET 2020"
17	<code>creator_name</code> = "DLR-DFD"
18	<code>creator_url</code> = "http://wdc.dlr.de"
19	<code>creator_email</code> = "wdc@dlr.de"
20	<code>project</code> = "Copernicus Climate Change Service (C3S) - European Centre for Medium-Range Weather Forecasts (ECMWF)"
21	<code>geospatial_lat_min</code> = -90.0
22	<code>geospatial_lat_max</code> = 90.0
23	<code>geospatial_lon_min</code> = -180.0
24	<code>geospatial_lon_max</code> = 180.0
25	<code>time_coverage_start</code> = "20080302000000"
26	<code>time_coverage_end</code> = "20080302235959"
27	<code>time_coverage_duration</code> = "240000"
28	<code>license</code> = "C3S-ECMWF Data Policy: free and open access"



29	<code>input_file_list = "D_DLR_IASI_DUST_v70_M02_20080302142059Z_20080302160258Z.nc , D_DLR_IASI_DUST_v70_M02_20080302092059Z_20080302110259Z.nc , ... "</code>
30	<code>start_date = "2008-03-02"</code>
31	<code>date_time = "2008-03-02 00:00:00" (UTC time of first observation)</code>
32	<code>platform = "Metop-A"</code>
33	<code>sensor = "IASI"</code>
Auxiliary variables	
1	<code>latitude</code> (at center; for level 3 vector with same value for each line of the data arrays, for level 2 also a complete vector with different values for each pixel)
2	<code>longitude</code> (at center; for level 3 vector with same value for each column of the data arrays, for level 2 also a complete vector with different values for each pixel)
3	<code>time</code> (UTC time of acquisition HHMMSS; one vector for level 2 with pixel acquisition times, two arrays with first and last time of acquisition of any contributing pixel for level 3)
Product variables for Level 3 (Products for Level 2 include all variables of the Generic IMARS output)	
4	<code>D_AOD10000</code> (dust AOD at 10µm)
5	<code>D_AOD11000</code> (dust AOD at 11µm)
6	<code>D_AOD550</code> (dust AOD at 0.55µm)
7	<code>D_retrieval_uncertainty</code> (early stage dust retrieval uncertainty)
8	<code>D_AOD10000_uncertainty</code> (dust AOD uncertainty at 10µm)
9	<code>D_AOD11000_uncertainty</code> (dust AOD uncertainty at 11µm)
10	<code>D_AOD550_uncertainty</code> (dust AOD uncertainty at 0.55 µm)
11	<code>D_probability</code> (dust probability)
12	<code>D_REFF</code> (dust effective radius; in µm)
13	<code>D_MWMD</code> (dust mass-weighted diameter; in µm)
14	<code>D_mass</code> (dust mass column; in g/m ²)
15	<code>D_temperature</code> (dust layer emission temperature; in K)
16	<code>D_quartz_fraction</code> (quartz abundance in dust; in %)
17	<code>D_illite_fraction</code> (illite abundance in dust; in %)
18	<code>D_kaolinite_fraction</code> (kaolinite abundance in dust; in %)
19	<code>D_montmorillonite_fraction</code> (montmorillonite abundance in dust; in %)
20	<code>D_feldspar_fraction</code> (feldspar abundance in dust; in %)
21	<code>D_calcite_fraction</code> (calcite abundance in dust; in %)
22	<code>COD550</code> (COD at 0.55µm)
Diagnostic variables	
22	<code>satellite_zenith</code> (at center)
23	<code>land_flag</code> (ocean (0) or land (1))
24	<code>cloud_fraction</code> (proportion of pixels with COD550 > 0.5 and CQF > 5)
25	<code>D_quality_flag</code> (increasing quality from 0 to 1)
26	<code>retrieval_entropy</code> (retrieval information content)
27	<code>number_of_dust_observations</code> (number of dust observations depending on quality filter)
28	<code>total_number_of_observations</code> (total number of observations)



4.3 Guidelines for product use: confidence levels

Table 11: Guidelines for application of different levels of quality filtering.

Confidence	Apply filters	Description	Suggested use
Highest level	$DQF > 3$ and $P_{dust} > 0.5$ and $H < 0.9$ and $\epsilon_{dust} < 0.4$	All quality control filters enabled, yields low number of observations, no interference with cloud contamination	Only if highest reliability level is required, for example: <ul style="list-style-type: none"> • aggregation of mineralogical information • deposition research • analysis of dust radiative effects
High level	$DQF \geq 3$ and $P_{dust} > 0.5$ and $H < 0.9$	Most quality filters enabled, yields moderately low number of good-quality observations, no interference with cloud contamination	for example: <ul style="list-style-type: none"> • Validation • data assimilation • climatology generation • case studies
Moderate level	$DQF \geq 3$ and $H < 0.9$	Uses aggregated quality flag and entropy, reasonable number of observations, no interference with cloud contamination	For example: <ul style="list-style-type: none"> • Aerosol-cloud-interaction research • case studies • near-real-time applications
Basic level	$AOD > 0$	Considers all dust observations, very high number of observations, potential interference with cloud contamination	for example: <ul style="list-style-type: none"> • manual selection • volcanic ash studies • case studies • retrieval development

The IMARS products are accompanied with a couple of variables for quality control. In general it is possible to use the basic quality level with no great risk due to the intrinsic quality assurance by the posteriori cloud discrimination scheme (see 5.5). Nevertheless, if one needs high quality observations, it is recommended to use a combination of restrictions for quality flag, dust probability, dust uncertainty and retrieval entropy. Selecting $DQF \geq 3$ discards observations with questionable quality. Further confinements with dust probability $P_{dust} \geq 0.5$ and retrieval entropy $H \leq 0.9$ increases the reliability of the dust retrieval significantly. If additionally $\epsilon_{dust} < 0.4$ (uncertainty of 40%) is selected, only the most reliable dust observations pass the quality filter. Table 11 summarizes these guidelines on quality filtering and how the filtering impacts on the selection of observations. All information required for applying tailored quality filtering is directly available from the IMARS files themselves.



References

- Ackerman, S.A.: Remote sensing aerosols using satellite infrared observations, *J. Geophys. Res.*, 102, 17069-17079, 1997.
- Acquista, C., Cohen, A., Cooney, J.A., Wimp, J.: Asymptotic behaviours of the efficiencies in Mie scattering, *J. Opt. Soc. Am.*, 70, 1023-1028, 1980.
- Aronson, J.R., Emslie, A.G., Smith, E.M., and Strong, P.F.: Infrared spectra of lunar soils and related optical constants, *Proc. Lunar Planet. Sci. Conf. 10th*, 1787-1795, 1979.
- Aronson, J.R.: Optical constants of monoclinic anisotropic crystals: orthoclase, *Spectrochimica Acta*, 42A, 187-190, 1986.
- Baum, B.A., Yang, P., Heymsfield, A.J., Bansemmer, A., Cole, B.H., Merrelli, A., Schmitt, C., and Wang, C.: Ice cloud single-scattering property models with the full phase matrix at wavelengths from 0.2 to 100 μm , *Journal of Quantitative Spectroscopy & Radiative Transfer*, 146, 123–139, doi: 10.1016/j.jqsrt.2014.02.029, 2014.
- Bohren, C.F., and Huffman, D.R.: *Absorption and scattering of light by small particles*, John Wiley & Sons, New York, USA, 1983.
- Caquineau, S., Gaudichet, A., Gomes, L., Magonthier, M.-C., and Chatenet, B.: Saharan dust: Clay ratio as a relevant tracer to assess the origin of soil-derived aerosols, *Geophys. Res. Lett.*, 25, 983-986, doi: <https://doi.org/10.1029/98GL00569>, 1998.
- Chýlek, P., Klett, J.D.: Absorption and scattering of electromagnetic radiation by prismatic columns: anomalous diffraction approximation, *J. Opt. Soc. Am. A*, 8(11), 1713-1720, 1991.
- Chýlek, P.: Asymptotic limits of the Mie-scattering characteristics, *J. Opt. Soc. Am. A*, 65, 1316-1323, 1975.
- Clarisse, L., Coheur, P.-F., Prata, F., Hadji-Lazaro, J., Hurtmans, D., and Clerbaux, C.: A unified approach to infrared aerosol remote sensing and type specification, *Atmos. Chem. Phys.*, 13, 2195-2221, doi: <https://doi.org/10.5194/acp-13-2195-2013>, 2013.
- De Leeuw, G., Holzer-Popp, T., Bevan, S., Davies, W.H., Descloitres, J., Grainger, R.G., Griesfeller, J., Heckel, A., Kinne, S., Klüser, L., Kolmonen, P., Litvinov, P., Martynenko, D., North, P., Ovigneur, B., Pascal, N., Poulsen, C., Ramon, D., Schulz, M., (...), Pinnock, S.: Evaluation of seven European aerosol optical depth retrieval algorithms for climate analysis, *Remote Sens. Environ.*, doi:10.1016/j.rse.2013.04.023, 2015.
- Deirmendjian, D.: *Electromagnetic Scattering on Spherical Polydispersions*, RAND Report R-456-PR, Elsevier, New York, 1969.
- Di Biagio, C., Boucher, H., Caquineau, S., Chevaillier, S., Cuesta, J., and Formenti, P.: Variability of the infrared complex refractive index of African mineral dust: experimental estimation and implications for radiative transfer and satellite remote sensing, *Atmos. Chem. Phys.*, 14, 11093–11116, doi:10.5194/acp-14-11093-2014, 2014.
- Formenti, P., Rajot, J.L., Desboeufs, K., Caquineau, S., Chevaillier, S., Nava, S., Gaudichet, A., Journet, E., Triquet, S., Alfaro, S., Chiari, M., Haywood, J., Coe, H., and Highwood, E.: Regional variability of the



composition of mineral dust from western Africa: Results from the AMMA SOP0/DABEX and DODO field campaigns, *J. Geophys. Res.*, 113, D003C134, doi: 10.1029/2008JD009903, 2008.

Glotch, T.D., Rossman, G.R., and Aharonson, O.: Mid-infrared (5-100 μ m) reflectance spectra and optical constants of ten phyllosilicate minerals, *Icarus*, 192, 605-622, doi: <https://doi.org/10.1016/j.icarus.2007.07.002>, 2007.

Hudson, P. K., Gibson, E.R., Young, M. A., Kleiber, P. D., and Grassian, V. H.: Coupled infrared extinction and size distribution measurements for several clay components of mineral dust aerosol, *J. Geophys. Res.*, 113, D01201, doi:10.1029/2007JD008791, 2008a.

Hudson, P. K., Young, M. A., Kleiber, P. D., and Grassian, V. H.: Coupled infrared extinction spectra and size distribution measurements for several non-clay components of mineral dust aerosol (quartz, calcite, and dolomite), *Atm. Environ.*, 42, 5991-5999, doi: [10.1016/j.atmosenv.2008.03.046](https://doi.org/10.1016/j.atmosenv.2008.03.046), 2008b.

v.d. Hulst, H.C.: Light scattering by small particles, Dover Publications, Inc., New York, USA, 1980.

Kandler, K., Schütz, L., Jäckel, S., Lieke, K., Emmel, C., Müller-Ebert, D., Ebert, M., Scheuvsens, D., Schladitz, A., Šegvić, B., Wiedensohler, A., and Weinbruch, S.: Ground-based off-line aerosol measurements at Praia, Cape Verde during the Saharan Mineral Dust Experiment: microphysical properties and mineralogy, *Tellus*, 63B, 459-474, doi: <https://doi.org/10.1111/j.1600-0889.2011.00546.x>, 2011.

Klüser, L., Banks, J.R., Martynenko, D., Bergemann, C., Brindley, H.E., and Holzer-Popp, T.: Information content of space-borne hyperspectral infrared observations with respect to mineral dust properties, *Remote Sensing of Environment*, 156, 204-309, doi:10.1016/j.rse.2014.09.036, 2015.

Klüser, L., Di Biagio, C., Kleiber, P.D., Formenti, P., and Grassian, V.H.: Optical properties of non-spherical desert dust particles in the terrestrial infrared – An asymptotic approximation approach, *J. Quant. Spectrosc. Radiative Transf.*, 178, 209-223, doi:10.1016/j.jqsrt.2015.11.020, 2016.

Klüser, L., Kleiber, P., Holzer-Popp, T., and Grassian, V.H.: Desert dust observation from space – Application of measured mineral component infrared extinction spectra, *Atm. Env.*, 54, 419-427, doi: [10.1016/j.atmosenv.2012.02.011](https://doi.org/10.1016/j.atmosenv.2012.02.011), 2012.

Lane, M.D.: Midinfrared optical constants of calcite and their relationship to particle size effects in the thermal emission spectra of granular calcite, *J. Geophys. Res.*, 104/E6), 14099-14108, doi: <https://doi.org/10.1029/1999JE900025>, 1999.

Laskina, O., Young, M.A., Kleiber, P.D., and Grassian, V.H.: Infrared extinction spectra of mineral dust aerosol: Single components and complex mixtures, *J. Geophys. Res.*, doi:10.1029/2012JD017756, 2012.

Legrand, M., Dubovik, O., Lapyonok, T. Derimian, Y., Accounting for particle non-sphericity in modeling of mineral dust radiative properties in the thermal infrared, *J. Quant. Spectrosc. Radiat. Transf.*, 149, 219-240, doi:10.1016/j.jqsrt.2014.07.014, 2014.

Lentz, W.J.: Generating Bessel functions in Mie scattering calculations using continued fractions, *Appl. Opt.*, 15, 668-671, 1976.

Long, L.L., Query, M.R., Bell, R.J., Alexander, R.W, Optical properties of calcite and gypsum in crystalline and powdered form in the infrared and far-infrared, *Infrared Phys.*, 34, 191-201, 1993.



- Mahowald, N.M., Kloster, S., Engelstaedter, S., Moore, J.K., Mukhopadhyay, S., McConnell, J.R., Albani, S., Doney, S.C., Bhattacharya, A., Curran, M.A.J., Flanner, M.G., Hoffman, F.M., Lawrence, D.M., Lindsay, K., Mayewski, P.A., Neff, J., Rothenberg, D., Thomas, E., Thornton, P.E., and Zender, C.S.: Observed 20th century desert dust variability: impact on climate and biogeochemistry, *Atm. Chem. Phys.*, 10, 10875-10893, doi: 10.5194/acp-10-10875-2010, 2010.
- Maslovska, A., Flatau, P.J., Stephens, G.L.: On the validity of the anomalous diffraction theory to light scattering by cubes, *Opt. Commun.*, 107, 35-40, 1994.
- Mogili, P.K., Yang, K.H., Young, M.A., Kleiber, P.D., and Grassian, V.H.: Extinction spectra of mineral dust aerosol components in an environmental aerosol chamber: IR resonance studies, *Atm. Env.*, 42, 1752-1761, doi: [10.1016/j.atmosenv.2007.11.026](https://doi.org/10.1016/j.atmosenv.2007.11.026), 2008.
- O'Neill, N.T., Ecki, T.F., Smirnov, A., Holben, B.N., and Thulasiraman, S.: Spectral discrimination of coarse and fine mode optical depth, *J. Geophys. Res.*, 108, D17, 4559, doi:10.1029/2002JD002975, 2003.
- Petty, G.W.: *A First Course in Atmospheric Radiation*, Sundog Publishing, Madison, Wisconsin, USA, 2006.
- Querry, M.R., *Optical constants of minerals and other materials from the millimeter to the ultraviolet*, US Army, Aberdeen, Md, USA, 1987.
- Rodgers, C.D.: *Inverse methods for atmospheric sounding, theory and practice*, Series on atmospheric, oceanic and planetary physics, vol.2, World Scientific Publishing, Singapore, doi: <https://doi.org/10.1142/3171>, 2000.
- Roush, T., Pollack, J., Orenberg, J., Derivation of midinfrared (5-25 μ m) optical constants of some silicates and palagonite, *Icarus*, 94, 191-208, 1991.
- Shannon, C.E., and Weaver, W.: *The Mathematical Theory of Communication*, University of Illinois Press, 1949.
- Shannon, C.E.: Communication in the Presence of Noise, *Proceedings of the IEEE*, 86, 2, 447-457, 1949.
- Sokolik, I.N., and Toon, O.B.: Incorporation of mineralogical composition into models of the radiative properties of mineral aerosol from UV to IR wavelengths, *J. Geophys. Res.*, 104, D8, 9423-9444, 1999.
- Spitzer, W.G., and Kleinman, D.A.: Infrared lattice bands of quartz, *Phys. Rev.*, 121, 1324-1335, doi:10.1103/PhysRev.121.1324, 1961.
- Wenrich, M.L., and Christensen, P.R.: Optical constants of minerals derived from emission spectroscopy: application to quartz, *J. Geophys. Res.*, 101, B7, 15921-15931, 1996.
- Yang, P., Feng, Q., Hong, G., Kattawar, G.W., Wiscombe, W.J., Mishchenko, M.I., Dubovik, O., Laszlo, I., and Sokolik, I.N.: Modeling of the scattering and radiative properties of nonspherical dust-like aerosols, *Journal of Aerosol Science*, 28, 995-1014, doi: 10.1016/j.jaerosci.2007.07.001, 2007.
- Yang, P., Wei, H., Huang, H.-L., Baum, B.A., Hu, Y.X., Kattawar, G.W., Mishchenko, M.I., and Fu, Q.: Scattering and absorption property database for nonspherical ice particles in the near- through far-infrared spectral region, *Appl. Opt.*, 44, 5512-5523, doi: <https://doi.org/10.1364/AO.44.005512>, 2005.



ECMWF – Robert-Schumann-Platz 3, D-53175 Bonn

Contact: <https://support.ecmwf.int/>